1   **Magnesium Facilitates the Healing of Atypical Femoral Fractures: A Single-cell**

2   **Transcriptomic Study**

3   Nianye Zheng[1,2,3,+], Jiankun Xu[1,2,+], Ye Chun Ruan[4], Liang Chang[1,2], Xinluan Wang[5], Hao

4   Yao[1,2], Jiali Wang[6], Ri Zhang[1,2], Qingyun Xue[7], Ning Tang[1], Tim-yun Ong[1], Jörg Schilcher[8,9],

5   Regis J. O'Keefe[3,*], Ling Qin[1,2,5,*]

6   [1] Musculoskeletal Research Laboratory of the Department of Orthopedics and Traumatology,

7   Faculty of Medicine, Chinese University of Hong Kong, HK SAR, PR China.

8   [2] Innovative Orthopedic Biomaterial and Drug Translational Research Laboratory, Li Ka Shing

9   Institute of Health Sciences, Chinese University of Hong Kong, Hong Kong SAR, PR China.

10   [3] Department of Orthopedic Surgery, Washington University School of Medicine, St. Louis, MO,

11   USA.

12   [4] Department of Biomedical Engineering, Faculty of Engineering, Hong Kong Polytechnic

13   University, Hong Kong, PR China.

14   [5] Translational Medicine R&D Center, Institute of Biomedical and Health Engineering, Shenzhen

15   Institutes of Advanced Technology, Chinese Academy of Sciences, Shenzhen, PR China.

16   [6] School of Biomedical Engineering, Sun Yat-sen University, Guangzhou, PR China.

17   [7] Department of Orthopedic Surgery, Beijing Hospital, Beijing, PR China.

18   [8] Department of Orthopedic Surgery, University Hospital Linköping, Linköping, Sweden.

19   [9] Wallenberg Centre for Molecular Medicine, Linköping University, Linköping, Sweden.

20

21

22   * Corresponding author. Email: qin@ort.cuhk.edu.hk (L.Q.); rokeefe@wustl.edu (R.O.)

23   + These authors contributed equally to this work.

Abstract: Bisphosphonates (BPs)-associated atypical femoral fractures (AFFs) present with impaired ==fracture== healing, yet the underlying mechanism is unclear, which prevents the development of effective therapy. Peripheral sensory nerve has been shown to regulate fracture healing via releasing neuropeptides. Here we show that long-term BPs pre-treatment leads to fracture non-union in rats characterized by reduced expression of calcitonin gene-related peptide (CGRP, a predominant type of neuropeptides) and abundant fibrous tissues in the non-bridged fracture gap, mimicking clinical AFFs. By using single cell mRNA-sequence, long-term BPs treatment was identified to promote transition of progenitor cells into a specific cluster of fibroblasts that actively deposit dense extracellular matrix (ECM) to prevent fracture callus bridging. Administration of exogenous CGRP at early stages of fracture repair, in contrast, eliminates the ECM-secreting fibroblast cluster, attenuates fibrogenesis, and facilitates callus bridging, suggesting CGRP is a promising agent to facilitate AFF repair. Accordingly, we have developed an innovative magnesium (Mg) containing hybrid intramedullary nail fixation system (Mg-IMN) that effectively stimulates rat fracture healing via elevating CGRP synthesis and release. Such device optimizes the fracture healing in BPs-pretreated rats, comparable to direct administration of CGRP. These findings address the indispensable role of CGRP in advancing the healing of AFFs and develop translational strategies to accelerate AFF healing by taking advantage of the CGRP-stimulating effect of Mg-based ==biodegradable== orthopedic implant. The study also indicates fibrosis could be targeted by augmenting CGRP expression to accelerate fracture healing even under challenging scenarios where fibroblasts are aberrantly activated.

Keywords: Atypical femoral fractures (AFFs); Bisphosphonates (BPs); Calcitonin gene-related peptide (CGRP); Magnesium (Mg); Single-cell mRNA sequencing

Graphic abstract
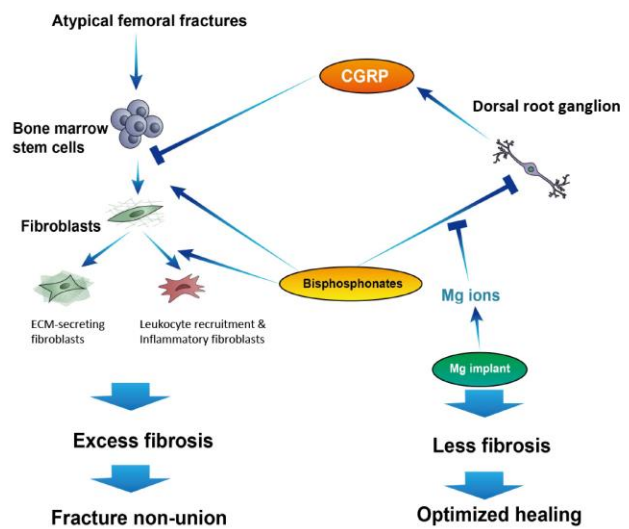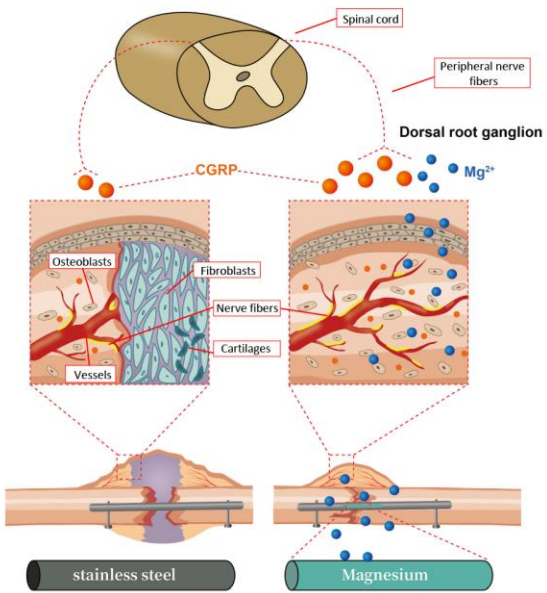
Introduction

Bisphosphonates (BPs) are popular anti-bone resorption drugs that are widely prescribed to treat osteoporosis and reduce the risk of osteoporotic fractures. Currently, over 4 million women over 45-year-old are taking these agents solely in the USA [1]. However, long-term use of BPs has been found to result in a new type of fractures, known as atypical femoral fractures (AFFs) [2,3]. The risk for AFFs increases with the duration of BPs treatment. Subjects taking BPs for 4 years are over 100 times more likely to develop AFFs as compared to the peers, with the age-adjusted incidence rate as high as 107.5/100,000 person-year for those with over 10 years administration [4,5]. Surgical fixation with intramedullary nail (IMN) is the mainstay for treating AFFs. Unfortunately, over 20-30% these cases, which is 2-3 times of that of femoral shaft fractures without BPs exposure, present with delayed fracture union or nonunion, many of which require secondary operations [6–9]. Apparently, novel therapeutic approaches are urgently needed to be developed to accelerate AFF healing.

The mechanism underlying the delayed healing of BPs-associated AFFs remains elusive. Bisphosphonates inhibit bone resorption via interfering with mevalonate pathway in osteoclasts [3]. When given after fractures, BPs or other anti-resorptive drugs have been proven safe to bone healing [10]. Similarly, transgenic rats with downregulated osteoclast function did not display fracture non-union [11], indicating the suppressed osteoclast activities *per se* does not impair AFF healing. In clinics, AFF patients retain normal bone formation capacities with upregulated osteoblastic differentiation potential of progenitor cells compared to BPs naïve subjects [12,13], again suggesting that delayed osteogenesis is unlikely the cause of defective AFF healing. At

84   present, the pathological impact of long-term BPs treatment on fracture healing remains unclear

85   and requires further investigation.

86

87   Bone tissues are densely distributed by peripheral nerve fibers, which in turn regulate skeletal

88   hemostasis by releasing neural factors, particularly calcitonin gene-related peptide (CGRP) [14].

89   During embryonic limb development, innervation of CGRP-positive nerve fibers precedes

90   vascular invasion, followed by mineralization to form the primary and secondary ossification

91   centers [15]. Similarly, at the early stage of fracture repair CGRP expression is elevated in the

92   fracture callus prior to vascularization and ossification in order to bridge the fracture gap [16,17].

93   These facts imply a pivotal role of CGRP in long bone homeostasis and regeneration potentially

94   by mediating angiogenesis and mineralization, especially in long bone shaft, which is the bony

95   region covered by periosteum. In support of this, depletion of CGRP has resulted in a lower bone

96   mass and impaired fracture healing [18,19], while supplementation of CGRP leads to facilitation

97   of fracture repair with enhanced osteogenic differentiation of periosteal osteoprogenitor cells via

98   stimulating G protein-coupled receptors (GPCR)/cAMP/protein kinase A pathway [19,20].

99   Moreover, CGRP can promote angiogenesis [20,21]. Of note, sensory nerve sprouting and CGRP

100 expression in bone tissues are reduced by BPs treatment as shown by pre-clinical evidence [22–

101 24]. Besides, BPs are shown to suppress angiogenesis both *in vitro* and *in vivo* [25,26]. On the

102 other hand, CGRP is known to promote angiogenesis, which has been proven crucial for bone

103 regeneration [27,28]. As such, long-term BPs exposure was hypothesized to inhibit AFF healing

104 via impairing CGRP-mediated angiogenesis-osteogenesis coupling. More importantly,

105 upregulating CGRP expression could be effective for expediting AFF healing. At the translational

106 aspect, we have developed a magnesium-containing intramedullary nail (Mg-IMN) fracture

107   fixation system that efficiently boosts endogenous CGRP by releasing Mg ions during implant

108   degradation *in vivo*, resulting in enhanced fracture repair in ovariectomy-induced osteoporotic rats

109   [19]. A more recent work demonstrates that Mg-based orthopedic implant increases the expression

110   of type-H vessels in bone tissues, which play indispensable role in coupling angiogenesis and

111   osteogenesis [27,29]. Therefore, it is proposed that Mg-IMN, as an internal fixation device, could

112   be particularly beneficial in enhancing AFF healing.

113

114   Here, we present the single cell mRNA-seq data characterizing the molecular and cellular features

115   of impaired fracture healing potential of AFFs. By establishing a rat fracture model with long-term

116   BPs pretreatment, a constellation of pathological features during fracture healing was revealed,

117   including reduced CGRP expression and alternated differentiation trajectory of osteoprogenitor

118   cells. Then, we observed an optimized healing outcome after supplementation of CGRP either

119   exogenously or endogenously via Mg-IMN implantation, suggesting CGRP is critically involved

120   in the defective tissue regeneration potential under the influence of BPs. Collectively, these

121   findings indicate that restoring CGRP expression during fracture healing could be a promising

122   strategy to accelerate AFF healing.

123

124   **Results**

125   ***Impaired fracture callus bridging in a rat model with long-term BPs treatment***

126   Since most AFFs occur in osteoporotic population, we first tested if long-term BPs treatment was

127   detrimental to osteoporotic fracture healing in animals. Ovariectomized (OVX) rats were subjected

128   to zoledronate (ZOL) treatment at a high (0.3 mg/kg/week for 3 months) or low dose (0.1 mg /kg/3

129   months for 6 months), followed by unilateral closed femoral fracture fixed with conventional

130   stainless-steel intramedullary nail (SS-IMN). In rats with high dose BPs pre-treatment, 62.5% of

131   animals showed non-bridged callus at 12 weeks post-fracture (wpf), as opposed to 44.4% and

132   16.7% in the low dose and the control group, respectively (Fig. S1, Table S1). As AFFs also

133   develop in non-osteoporotic patients prescribed with high dose BPs for treating cancers [30], we

134   next administrated high dose ZOL (0.3mg/kg/week for 3 months) to non-OVX rats, which

135   subsequently produced a more consistent phenotype of delayed union with a callus non-bridging

136   rate as high as 94% at 12 wpf (Fig. 1A and 1B, Table S2). By 24 wpf, around 90% of ZOL group

137   animals showed non-bridged callus, which is defined as fracture non-union (Fig. 1A). These data

138   indicate that BPs treatment may produce an unfavorable microenvironment that impairs fracture

139   healing regardless of osteoporotic status. OVX-induced osteoporotic status might partially

140   optimize the ZOL-impaired healing as compared to non-OVX rats, which could be explained by

141   upregulated osteoclast activities secondary to estrogen deficiency. To maximize the potential

142   detrimental effect of BPs, the delayed healing model, i.e. 3 months ZOL treatment at a dose of 0.3

143   mg/kg/week prior to fractures in non-OVX rats, was used in the subsequent studies.

144

145   It is generally appreciated that, when fixation is stable, the major cause of impaired fracture healing

146   is biological factors, such as reduced bone forming capacities [31]. However, the hard callus

147   volume of our non-union model was "paradoxically" higher than that of the control group at as

148   early as 4 wpf (Fig. 1C, 1D), suggesting that osteogenesis was enhanced rather than inhibited.

149   Similar to clinical observations [32], the progenitor cells isolated from ZOL group before and after

150   fractures (Fig. 1E) also displayed dramatically increased osteogenic potential compared to the

151   control (Fig. 1F, 1G), indicating that the poor healing outcome of AFFs may not be attributed to

152   the suppressed osteogenesis. Instead, other unrecognized mechanisms may be involved.

153

Fibrosis and abnormal vessels within the non-bridged fracture gap

We next characterized the pathological features of the fracture site in BPs-induced non-union. In rats without BPs injection (control group), typical intramembranous and endochondral ossification were observed at the distal ends and center of the fracture gap, respectively, at 4 wpf. At this time point, in contrast, ZOL group displayed abundant fibrous tissues in the fracture gap, with 20% of the rats showing no cartilaginous structures (Fig. 2A). At 12 wpf, the fracture gap in the control group was bridged by hard callus. The ZOL group, however, still presented with abundant fibrous tissues interposed between the fracture ends, where T (Cd3 positive) and B (Cd19 positive) lymphocytes were identified (Fig. 2B). Compared to the control group, ZOL group showed increased immunofluorescent intensities of Cd26-positive fibroblasts (Fig. 2C), some of which co-express Cd10, a marker of cancer-associated fibroblasts involved in cancer development and chemoresistance [33]. The vessels in the fracture gap of ZOL group were disorganized and abnormally large in diameter while low in density and connectivity at 3 wpf (Fig. 2D, upper panel). At 8 wpf, ZOL group showed retention of vessels-like structures, a part of which stained positive for alpha-smooth muscle actin (α-SMA, Fig. 2D, lower panel). Interestingly, stronger periosteal response with bulky hard callus formation was observed as early as 2 wpf (Fig. 2A), which again indicated increased osteogenesis as osteoclast-mediated bone resorption was too early to occur at this stage. Of note, such collection of histological features recapitulated that of the fracture gap of human AFFs after long-term BPs exposure (Fig. 2E), where the external callus was interrupted by fibrous tissues when approaching the fracture gap. Between the fractured cortices were amorphous acellular materials and cortical fragments. In addition, the fibrosis within the fracture gap was smoothly connected to bone marrow cavity. These suggest our animal model is clinically relevant.

176 Though such phenotype of non-union closely mimics that of classic hypertrophic fracture non-

177 unions in clinics [34], the underlying mechanism may be different because classic hypertrophic

178 fracture non-unions are induced by poor fixation or high strains in the fracture gap, which is not

179 the case in AFFs. On the other hand, bone formation capacity in AFFs, as one of the major

180 determinants ensuring successful fracture healing, is "paradoxically" increased. These findings

181 collectively support that the aberrant fibrosis and angiogenesis may be the key contributors to long-

182 term BPs treatment-induced non-union of AFFs.

183

184 Of note, apart from excess fibrosis, most rats in ZOL group (80%) additionally showed retention

185 of cartilaginous tissues at the late stages of fracture healing (Fig. 2F, Fig. S2A). The

186 glycosaminoglycans (GAGs)-rich area stained by safranin O was minimal at 4 wpf, at which time

187 fibrosis was the most prominent. At 8 wpf, the GAG-rich area slightly increased, and remained

188 unchanged till 24 wpf (Fig. 2G). During the same period, the chondrocyte-like cells underwent a

189 gradual transition from hyaline cartilage to fibrocartilaginous tissues, which displayed the distinct

190 spindle shape and were smoothly connected to the peripheral mesenchymal fibrous tissues (Fig.

191 2F, Fig. S2B). These results suggest that the fibrous tissues may be an important niche that favors

192 the appearance of fibrocartilages or prevents endochondral ossification.

193

194 ***ZOL prevented the clearance of collagen-secreting fibroblasts***

195 To dissect the mechanism of the fibrotic fracture non-union, we first measured the fraction of

196 fibroblasts in the soft callus. Flow cytometry was performed on single-cell suspension of fracture

197 callus cells (FCCs) obtained from enzymatical digestion of callus tissues harvested at different

198 time points of fracture healing (Fig. 3A). S100a4 (i.e. fibroblast-specific protein-1) and Cd26 were

199 chosen as markers for mature fibroblasts [35]. Particularly, Cd26 has been shown to be pathogenic

200 to fibrosis development in rodent liver and kidney [36,37]. As a result, a higher proportion of

201 S100a4/Cd26 double-positive fibroblasts among all FCCs was found in ZOL group at 4 wpf as

202 compared to the control group (7.7% vs 5.14%, Fig. 3B). At 12 wpf, these pathological fibroblasts

203 were mostly cleared (0.18%) with concurrent bony union of the fracture callus in the control group,

204 whereas ZOL-treated rats showed retention of these cells (6.03%), consistent with histological

205 findings (Fig. 2).

206

207 To resolve the genetic heterogeneity of the fibroblasts, we next performed single-cell mRNA

208 sequence (scRNA-seq) of the unfractioned adherent FCCs (Fig. 3A). Analysis showed that the

209 FCCs were fibroblasts as they all expressed known fibroblast genes (Fig. 3C, Fig. S3-S5). Of note,

210 both ZOL and the control group showed a cluster of fibroblasts that were enriched for genes

211 associated with collagen synthesis (e.g. *Col1a*, *Col3a1*, *Col5a2*, and *Col11a1*) (Fig. 3C, Fig. S3-

212 S5). Gene ontology (GO) analysis further suggested such population was specialized for producing

213 extracellular matrix (ECM) (Fig. S6). These ECM-producing cells were likely terminally

214 differentiated as they expressed low level of proliferative markers (*Ki67* and *Cdk1*) (Fig. S5B) and

215 resided at the distal end of developmental trajectory on pseudo-time analysis (Fig. S7). Notably,

216 the percentage of such unique cluster within the FCCs decreased by 24% on 12 wpf relative to 4

217 wpf in the control group, while increased by 20% in the ZOL group over the same period,

218 suggesting that the ECM-secreting fibroblasts may be associated with the fracture gap occupied

219 with fibrotic tissues (Fig. 3D). Immunofluorescent staining confirmed an increased expression of

220 collagen 3 in the fracture callus of ZOL group at 12 wpf compared to the control group (Fig. 3E).

221 Together, these data suggest that ZOL treatment may hamper the clearance of a distinct fibroblast

cluster that is actively secreting collagen to prevent callus bridging. Interestingly, combined analysis of scRNA-seq data revealed that ZOL treatment significantly downregulated the expression of *Fam111a* and *Mgp*, while elevated that of *Thbs4* in all fibroblast populations as compared to the control group at 4 wpf (Fig. S8A). The proteins encoding by the aforementioned genes are involved in either bone homeostasis or fibrosis [38–40].

ZOL promoted differentiation of myeloid progenitor cells into fibroblasts

It has been reported that around 11% of fibroblasts in the healing skin wound in mice were of myeloid origin [41]. Similarly, fibroblasts in both the control and ZOL group expressed myeloid-specific marker *Cd14* and/or *Lyz2* (Fig. S8B). Additionally, the fibrous tissues were connected to the bone marrow cavity (Fig. 3F). Therefore, we postulated that ZOL might facilitate the transition of myeloid progenitor cells into fibroblasts. In support of this, the fraction of myeloid-derived fibroblasts (*Cd14* positive) in the control group decreased from 23.55% at 4 wpf to 14.97% at 12 wpf as indicated by scRNA-seq, and a similar trend was observed specifically for the collagen-secreting clusters (Fig. 3G). In ZOL group, however, the proportion of the *Cd14*-positive fibroblasts remained unchanged over time (Fig. 3G). Immunohistochemistry staining validated that the fibrous tissues in ZOL group was positively stained for myeloid marker Cd68 and Cd14 [42], indicating a continuous contribution of myeloid cells to the development of fibrosis (Fig. 3H). Of note, ZOL group contained a unique cluster of fibroblasts which was over-represented in categories associated with myeloid leukocytes migration/regulation on GO analysis (Fig. 3I), echoing the histological features of chronic inflammation (Fig. 2B). These inflammation-related fibroblasts were particularly enriched for myeloid marker *Cd14* as well (Fig. 3I), suggesting a pathogenic role of bone marrow in the fracture non-union. Indeed, BMSCs from the fractured

245 femora at 4 wpf in ZOL group displayed dramatically increased fibrogenic potential on day 11 of

246 induction compared to those from the control rats, as evidenced by the increased collagen 3 and

247 Cd10 expression and upregulated *Hsp47* and *Col1a* gene expression level (Fig. 3J, left panel).

248 Further, *in vitro* treatment of BMSCs from the control rats with ZOL also increased fibrogenic

249 potential of the progenitor cells, supporting a direct effect of BPs on fibrotic changes (Fig. 3J, right

250 panel).

251

252 ***Decreased CGRP expression in AFFs***

253 We next suspected that CGRP was involved in the delayed healing of AFFs. Indeed, the fibrotic

254 fracture site of human BPs-induced AFFs displayed downregulated CGRP expression compared

255 to the age-matched BPs-naïve fracture patients (Fig. 4A, upper panel). Similar results were

256 observed in ZOL-pretreated rats at 4 wpf (Fig. 4A, lower panel), though the expression of CGRP

257 receptor calcitonin receptor like receptor (Crlr) and receptor activity-modifying protein (Ramp1)

258 were upregulated as a reflection of negative feedback (Fig. S9). These data, together with previous

259 pre-clinical studies [22–24], suggest that CGRP expression is inhibited by BPs. Interestingly, at 8

260 wpf the fibrous tissues in the gap of ZOL-treated animal heavily stained for CGRP (Fig. S10). This

261 might manifest chronic inflammation echoing the co-existence of lymphocytes (Fig. 2B). In fact,

262 CGRP is shown to involve in neuroinflammation [43]. Therefore, the upregulated CGRP at later

263 stages of AFF healing may not play an active role in promoting fracture healing. As it was

264 demonstrated in our previous study that CGRP enhanced fracture healing by acting on progenitor

265 cells [19], we next performed flow cytometry to assess if the number of CGRP-bound progenitor

266 cells were influenced by BPs treatment. Cd105 was chosen because it is a well-known progenitor

267 cell surface marker [44]. In the control group, the fraction of CGRP/Cd105 double-positive cells

268 peaked at 8 wpf (Fig. 4B), consistent with previous observation showing that CGRP only

269 participated in the early stage of fracture healing [17]. Compared to the control group, ZOL-treated

270 rats showed less CGRP-bound progenitor cells at 4 (5.9% vs 9.2%) and 8 wpf (11.2% vs 24.1%),

271 while more at 12 wpf (6.77% vs 0.20%), indicating BPs inhibited CGRP expression in the early

272 stage of fracture healing.

273

274 As CGRP is mainly released from sensory nerve endings, we next assessed CGRP expression in

275 sensory neurons in the dorsal root ganglia (DRGs) using our established protocol [19].

276 Immunofluorescent staining showed that CGRP in DRGs was lower in ZOL group relative to that

277 in the control group (Fig. 4C, upper panel), consistent with previous findings reporting that

278 biweekly systemic injection of ZOL significantly reduced the proportion of CGRP-positive

279 neurons (-54.6%) in the DRG of rats with monosodium iodoacetate-induced osteoarthritis [45].

280 Such BPs-induced downregulation of CGRP could be explained by dysregulated macrophages-

281 guided innervation [22]. Apart from this, ZOL may also directly inhibit CGRP production in DRGs

282 as evidenced by our *in vitro* data (Fig. 4C, lower panel) as well as others [23].

283

284 ***Restoration of CGRP to optimize ZOL-induced delayed fracture healing***

285 To assess if supplementation of CGRP could attenuate the impaired healing potential, we next

286 injected exogenous CGRP to the fracture site of ZOL-pretreated rats on a daily basis for 14 days

287 immediately after fractures. The regimen was chosen to be 100 μl/day (100 nM) for 14 days

288 because our previous studies showed neither a higher dose nor a longer duration further promoted

289 bone formation in rats [19,46]. Injection of CGRP to ZOL-treated rats (CGRP group) narrowed

290 the fracture gap and decreased callus non-bridging rate at 8 (58% vs 94%) and 12 wpf (50% vs

291 90%) compared to ZOL group without CGRP treatment (Fig. 4D and 4E, Table S3). In the control

292 group, the non-bridging rate was 0% and 17% at 8 and 12 wpf, respectively. There was significant

293 elevation in BV/TV (>8.5%, P = 0.0156) and BMD of TV (>11.2%, P = 0.0240) after CGRP

294 treatment compared to ZOL group at 12 wpf (Fig. 4F), suggesting that bone formation was

295 enhanced by CGRP. These data collectively support a beneficial role of CGRP in promoting the

296 fracture healing of ZOL-pretreated rats.

297

298 CGRP injection increased the number of CGRP/Cd105 double-positive cells in the fracture gap

299 compared to ZOL group at 4 (13.5% vs 5.89%) and 8 wpf (18.1% vs 11.2%) (Fig. S11).

300 Concurrently, the fraction of pathological fibroblasts (S100a4/Cd26 double-positive) declined

301 from 6.03% to 1.42% at 12 wpf (Fig. 4G), and collagen 3 expression was reduced as well (Fig.

302 4H), suggesting CGRP effectively attenuated the formation of fibrous tissues potentially by acting

303 on progenitor cells. We next performed scRNA-seq of the fracture callus cells isolated from CGRP

304 group at 4 and 12 wpf. Similar to the control and ZOL group, all the cells from CGRP-treated rats

305 were designated as fibroblasts based on the gene expression profile (Fig. S12, S13A). Specifically,

306 the collagen-rich fibroblasts cluster, which had been characterized in the control and ZOL group,

307 also existed in CGRP group rats (Fig. 4I). The majority (77.30%) of such collagen-secreting

308 fibroblasts in CGRP group at 4 wpf were cleared by 12 wpf, as opposed to a 19.50% increase in

309 ZOL group (Fig. 4J) over the same period, indicating that CGRP may decrease the production of

310 the committed ECM-secreting fibroblasts or enhance their clearance.

311

312 We further explored whether the reduction in fibroblasts number was due to inhibited

313 transformation of myeloid-derived progenitor cells into the fibroblasts. scRNA-seq data showed

that the fraction of myeloid-derived fibroblasts (*Cd14* expressing) in CGRP-treated rats dropped from 19.30% at 4 wpf to 15.57% at 12 wpf, while remained unchanged at around 20% in ZOL group (Fig. 4K, right panel). A similar trend was observed among ECM-secreting fibroblasts (Fig. 4K, left panel). In contrast to ZOL group which comprised a distinct myeloid-derived fibroblasts cluster that potentially contributed to the inflammatory phenotype in non-bridged fracture gap (Fig. 3I), such cluster disappeared after CGRP injection based on GO analysis (Fig. S13B). We next isolated primary BMSCs from the fractured femora of CGRP-treated rats at 4 wpf and performed fibrogenic induction *in vitro*. Progenitor cells from CGRP group showed increased CGRP expression, while decreased expression of fibrogenic marker Cd10 and collagen 3 (Fig. 4L, left panel). Additionally, gene expressions of *Hsp47* and *Col1a* were downregulated by CGRP treatment (Fig. 4L, right panel). It was noted that CGRP treatment also abrogated the ZOL-induced upregulation in osteogenic potential of BMSCs, and a similar trend was observed regarding adipogenesis (Fig. S14). Therefore, CGRP may play an important role in preventing pathological differentiation and maintain stemness of progenitor cells.

Optimized fracture healing by magnesium-containing intramedullary nail (Mg-IMN)

Given that our innovative Mg-IMN effectively enhanced osteoporotic fracture healing via stimulating CGRP release from sensory nerve endings [19], we postulated that such internal fixation implant with biodegradable Mg might also promote AFF healing. To test this hypothesis, we applied Mg-IMN instead of stainless steel IMN (SS-IMN) to fix unilateral closed femoral fractures in rats with ZOL pre-treatment for 3 months before fracture. Mg-IMN fixation stimulated callus formation at 4 wpf as indicated by the large external callus and increased callus area (Fig. 5A, 5B). At 12 and 24 wpf, rats fixed with Mg-IMN (Mg group) displayed vague fracture lines

337   and smoothly connected external radiopaque calluses, whereas those with SS-IMN fixation (ZOL

338   group) still showed non-bridged calluses (Fig. 5A, 5C). Radiograph-based assessment revealed

339   that Mg-IMN effectively reduced fracture non-bridging rate by 27.7% (68% vs 94%) at 8 wpf,

340   45.9% (53% vs 98%) at 12 wpf, and 35.2% (57% vs 88%) at 24 wpf compared to conventional

341   SS-IMN (Fig. 5D, Table S4). These data support a beneficial role of Mg-IMN in facilitating

342   fracture callus bridging of AFF animal model.

343

344   µCT analysis demonstrated that Mg-IMN significantly increased bone volume (BV) by 20.7% and

345   bone mineral content (BMC) of BV by 17.9% at 12 wpf compared to ZOL group (Fig. 5E).

346   Moreover, BMC of total volume (TV) was 18.1% higher in Mg group than in ZOL group (P <

347   0.05), suggesting that bone formation was enhanced by Mg-IMN. One explanation for this could

348   be the anti-fibrotic effect of CGRP, which enabled the replacement of fibrous tissues with

349   mineralized bone. Aside from this, Mg ion-induced CGRP release might also directly stimulate

350   osteogenesis of periosteum osteoprogenitor cells by acting on GPCR/PKA signally pathways [19].

351   Of note, direct delivery of CGRP resulted in a significantly increased BV/TV (+ 8.5%, P < 0.05)

352   and a trend of higher BV at 12 wpf (+ 8.5%, P = 0.5077) compared to ZOL group (Fig. 4F).

353   Moreover, both Mg-IMN and direct CGRP injection achieved a comparable reduction in callus

354   non-bridging rate compared to those without treatment at 12 wpf. These results suggest that Mg-

355   IMN promotes fracture healing via enhancing local CGRP release.

356

357   Histologically, Mg-IMN-treated rats displayed fewer fibrous tissues as well as optimized vessel

358   structures in the fracture gap compared to ZOL group (Fig. 5F, 5G). Flow cytometry showed that

359   there was a 36.7% reduction in pathological fibroblast fraction in Mg group at 4 wpf and 80.8% at

360 12 wpf relative to ZOL group (Fig. 5H). Mg-IMN also optimized the temporal distributive pattern

361 of cartilaginous tissues-rich area as indicated by safranin O (SO) staining (Fig. 5I). Compared to

362 ZOL group, more cartilages were discerned in Mg group at 4 wpf (+169.3%, P = 0.5276). By 24

363 wpf, Mg group showed no observable endochondral formation while ZOL group still presented

364 with persistent SO-stained region, indicating increased cartilage turnover accompanied with the

365 release of Mg ions. These data collectively suggest that degradation of Mg effectively mitigates

366 ZOL-induced fibrosis and, as a consequent, possibly attenuates retention of abnormal

367 fibrocartilages. Next, we performed scRNA-seq of fracture callus cells isolated form Mg-treated

368 rats at 4 and 12 wpf. Although the distinct ECM-secreting cluster (cluster 5 and 8 for week 4 and

369 week 12, respectively) still existed in Mg-treated rats (Fig. S16, S17A), the clearance of these cells

370 was significantly enhanced compared to ZOL group by 24 wpf (Fig. 5J). Of note, Mg ions reversed

371 the effect of ZOL on the gene transcriptions of *Fam111a*, *Mgp*, and *Thbs4*, all of which were

372 potentially involved in fibrosis and bone development (Fig. S17B) [38–40]. While myeloid

373 progenitor cells played an essential role in the delayed fracture healing of AFFs (Fig. 3), the

374 fraction of myeloid-derived fibroblasts (*Cd14* positive) in the fracture gap dropped by 12.75% in

375 rats treated with Mg (Fig. 5K). In addition, the unique cluster found in ZOL-treated rats, which

376 was originated from bone marrow and associated with inflammation, was absent after fracture

377 fixation with Mg-IMN at 12 wpf on GO analysis (Fig. S18). BMSCs isolated from Mg-IMN treated

378 rats at 4 wpf showed reduced fibrogenic potential as shown by reduced expression of collagen 3

379 and myeloid marker Cd10 (Fig. 5L). In addition, Mg treatment achieved a comparable reduction

380 in gene expressions of *Hsp47*, *S100a4*, and *Col1a as CGRP* did when compared to the control

381 group. Similar to CGRP group, Mg-IMN also attenuated ZOL-induced enhanced osteogenesis and

382 adipogenesis of BMSCs (Fig. S19). These data together denote that Mg-IMN prevents fibrogenic

383 differentiation of myeloid cells via upregulating CGRP, resulting in optimized vessel formation

384 and callus bridging (Fig. 5M).

385

386 To confirm the role of CGRP in the Mg-facilitated healing, we first measured CGRP expression

387 in Mg-IMN-fixed rats. Mg-IMN prominently reversed the ZOL-induced reduction in CGRP

388 expression in both the fracture callus and DRGs (Fig. 6A). Additionally, CGRP receptor Crlr was

389 further upregulated after Mg-IMN treatment (Fig. S9). In Mg-IMN group, the fraction of

390 CGRP/Cd105 double-positive cells was elevated to 8.58% and 29.3% at 4 and 8 wpf, respectively,

391 as compared to 5.89% at 4 wpf and 11.2% at 12 wpf in ZOL group (Fig. 6B). These results suggest

392 Mg-IMN effectively upregulated CGRP expression in ZOL-pretreated rats. Next, we transfected

393 ZOL-pretreated and Mg-IMN-fixed rats with adenovirus carrying anti-*Ramp1* shRNA (AdV-

394 sh*Ramp1*) or scramble sequence as the controls (scramble group) three days before fractures to

395 knock down CGRP receptor Ramp1. There was no apparent difference in either callus non-

396 bridging rate or healing patterns between scramble and Mg-IMN group, suggesting RNA

397 interference did not affect the healing outcome. By contrast, AdV-sh*Ramp1* abrogated the

398 beneficial effects of Mg-IMN in promoting radiographic healing outcome of ZOL-pretreated rats

399 (Fig. 6C, Table S5). At 8 wpf, *Ramp1* knockdown (KD) led to a higher callus non-bridging rate

400 compared to ZOL group (87.5% vs 54%,), approaching to that of ZOL group (94%) (Fig. 6D). At

401 12 wpf, the *Ramp1* KD group showed a slightly reduced non-union rate (70%) and a narrower

402 fracture gap compared to ZOL group (98%, Fig. 1B), possibly attributed to the fact that transfected

403 anti-*Ramp1* shRNA only expressed within a specific time window in the target cells, because

404 adenovirus delivered genes exist extra-chromosomally [47]. Quantitative analysis of X-ray

405 showed that both callus area and callus width in *Ramp1* KD group were significantly lower than

406 that in the scramble group at 4 and 8 wpf (Fig. 6E), suggesting that CGRP receptor Ramp1 was

407 required for callus formation in Mg-IMN-treated AFF rat model. Histologically, Ramp1 KD group

408 displayed a non-union phenotype similar to that of ZOL group with conventional SS-IMN fixation.

409 Collagen 3 expression was increased in the fracture gap of *Ramp1* KD rats compared to the

410 scramble group at 12 wpf (Fig. 6F). Meanwhile, the retained fibrosis tissues in rats with *Ramp1*

411 KD were positively stained for myeloid markers Cd68 and Cd14 (Fig. 6G). These data collectively

412 indicate that the beneficial effect of Mg-IMN in accelerating AFF healing is most likely mediated

413 by Mg ion-triggered CGRP release, which in turn prevents fibrosis via inhibiting fibrogenic

414 transformation of myeloid progenitor cells.

415

416 **Discussion**

417 The present study, by establishing a rat model of delayed fracture healing that phenocopied clinical

418 AFF specimens, reveals that BPs treatment suppresses CGRP expression and impairs fracture

419 union by generating aberrant fibrous tissues at the fracture gap (Fig. 7). To the best of our

420 knowledge, it is the first time scRNA-seq was applied to identify that ZOL can shunt the fate of

421 myeloid progenitor cells toward fibroblasts that actively secreted extracellular matrix and

422 subsequently impeded fracture union. Conversely, replenishing exogenous or endogenous CGRP

423 by surgical fixation with Mg-IMN attenuated the unfavored effect of ZOL on fibroblast population,

424 resulting in prominently decreased fracture non-union rate. A translational approach to enhance

425 AFF healing by using Mg-IMN has been validated with appreciation of the previously un-

426 recognized anti-fibrotic effect of CGRP. More importantly, eliminating fibroblasts by magnesium-

427 based biometal could be a novel therapeutic approach to accelerate fracture healing/bone

428 regeneration where over-activated fibroblasts are involved [48–50].

429

We compared clinical AFF specimens to those of animals and demonstrated that the key

pathological feature of zoledronate-induced delayed fracture healing was the abundant fibrotic

tissues interfering with the bridging of large external bony callus. We identified that fibrosis was

the cause, rather than the result, of delayed fracture healing considering direct osteogenesis was in

fact enhanced in zoledronate-treated rats. In addition, ZOL prevented the clearance of a unique

population of fibroblasts that were actively depositing ECM in the non-bridged fracture gap, and

strategies halting fibrogenic differentiation of BMSCs resulted in better healing outcome. Of note,

available evidence indicated that fibroblasts could directly inhibit osteogenic differentiation of

osteo-progenitor cells by secreting fibroblast activation protein [51]. Thus, the aberrant fibroblasts

may not only be a physical barrier but also provide an unfavorable biological niche for AFF repair.

440

The origin of the aberrantly distributed fibroblasts is believed to be bone marrow progenitors

(BMSCs) based on the following evidence. Firstly, fibrotic cells in the fracture gap were smoothly

connected to bone marrow cavity on histological sections. Secondly, an increased number of

fibroblasts expressing myeloid markers (e.g. *Cd14*) were observed in rats with ZOL pretreatment

compared to the control. Thirdly, BMSCs isolated from ZOL group rats showed dramatically

increased fibrogenic potential. As such, long-term ZOL treatment may promote fibrogenic

transition of BMSCs, leading to fibrotic fracture non-union. In line with this, a previous study

showed that around 11% fibroblasts in skin wound healing were of myeloid origin [41]. It is

traditionally believed that periosteum derived stem cells (PDSCs) are the dominant progenitor cell

type mediating fracture healing [52–54]. In contrast, the current study demonstrates BMSCs are

the major contributor to the prominent fibrosis impending fracture healing, suggesting an intrinsic

452   difference in the biological response to BPs treatment between these two progenitor cell types that

453   is worthy of further investigation. Though the depletion of CGRP by long-term BPs treatment

454   diverts the fate of bone marrow-derived stem cells into fibroblasts, the exact role of CGRP in this

455   process needs to be investigated, particularly on the potential involvement of cAMP/PKA/CREB

456   signaling pathway that is activated by CGRP receptor Ramp1 [19]. Li et al. found that denervation

457   of CGRP-enriched sensory nerves exacerbates bleomycin-induced pulmonary fibrosis in rats, and

458   CGRP hampers TGF-beta1-induced stimulation of ERK1/2-eIF3a pathway in fibroblasts, resulting

459   in inhibited fibroblasts proliferation *in vitro* [55]. This suggests TGF-beta1/ERK pathway may

460   also mediate the anti-fibrosis effect of CGRP. Besides, CGRP also acts via Sonic hedgehog

461   pathway to reduce the generation of reactive oxygen species (ROS), protecting lung epithelium

462   from hypoxia-induced damage [56]. As ROS could signal downstream of TGF-beta to stimulate

463   fibroblasts proliferation and ECM deposition, CGRP may additionally act as an antioxidant to

464   attenuate fibrosis in AFFs [57–59]. Interestingly, Mg-IMN not only reduced the degree of fibrosis

465   but also reversed the ZOL-induced reduction in gene expression level of *Fam111a*, *Mgp*, while

466   elevation of *Thbs4* in fibroblasts (Fig. S8A, S17B). *Fam111a* encodes a replication fork protein

467   Fam111a, the loss-of-function of which is associated with impaired skeletal development and a

468   phenotype mimicking congenital parathyroid hormone (PTH) deficiency [40]. *Mgp* encodes

469   Matrix GLA Protein, the knockout of which induces short stature, fractures, and spontaneous

470   calcification [38]. *Thbs4* encodes extracellular protein thrombospondin 4, which is involved in

471   stimulating fibroblast proliferation and promoting tumor invasion and metastasis [39]. Though the

472   exact roles of these genes in Mg-facilitated healing remain unknown, their close connection to

473   musculoskeletal system suggests that fibroblasts may directly regulate bone homeostasis and

474   regeneration via yet-to-be illuminated ways.

Apart from acting on CGRP, BPs are postulated to directly stimulate fibrosis via inducing inflammation. Indeed, BPs are found to be capable of stimulating fibroblasts by depleting anti-oxidant coenzyme Q, upregulating ROS level, and as a result promoting ECM secretion via facilitating NLRP-inflammasome-mediated IL-1beta production [60–63]. Statins, a class of anti-dyslipidemia drug with similar mechanism of action as BPs, aggravate bleomycin-induced lung fibrosis via the same mechanism [58]. Interestingly, the pro-fibrotic effect of statins is dependent on a pre-existed inflammatory status, either by bleomycin-induced lung injury *in vivo* or lipopolysaccharides (LPS)-induced macrophage activation *in vitro* [58]. For individuals without underlying pulmonary conditions, statins are safe. Similarly, BPs do not lead to fibrosis in intact femora because there lacks an inflammatory niche. After fractures, BPs may upregulate ROS level in the activated macrophages/osteoclasts or fibroblasts. The escalating amounts of ROS in turn stimulates macrophages to produce more IL-1beta, resulting in hyper-proliferation of fibroblasts and fibrosis [64]. In support of this, both the histology of our delayed healing AFF animal model and that of BPs-induced osteonecrosis of the jaw (BPONJ) showed signs of chronic inflammation [64]. Of note, the excess inflammation-induced fibrosis may also be pathogenic to other types of impaired fracture healing, such as those with chronic obstructive pulmonary disease, diabetic mellites, rheumatoid arthritis, and polytrauma [49,50]. Accordingly, Mg-based biomaterials may be effective for treating these disorders as well.

In summary, our work demonstrates that the underlying mechanism of impaired fracture healing potential of AFFs involves a suppressed CGRP expression in fracture sites after long-term BPs exposure. Preventing aberrant fibrotic differentiation of BMSCs via Mg-induced CGRP release

effectively mitigates aberrant fibrosis and, as a result, facilitates fracture healing in rats pre-treated with ZOL. Because Mg-based biodegradable materials have been used clinically in orthopedics with proven safety profile and osteo-anabolic effect [65,66], an important future direction will be the translational application of Mg-containing hybrid IMN system capable of continuous release of Mg ions to accelerate fracture healing of AFFs in clinics. Last but not the least, we also identify a unique fibroblast population that is detrimental to fracture healing. Such aberrant fibroblasts could be a common pathological factor contributing to impaired fracture repair and bone regeneration, particularly under excess inflammation [50]. As such, a promising future direction of clinical translation research would be to extend the indication of innovative and bioactive Mg-IMN for application in musculoskeletal conditions associated with excessive fibrosis.

Materials and Methods

Human Fracture Specimens

Clinical specimens of incomplete atypical femoral fracture were obtained from Department of Orthopedic Surgery, University Hospital Linköping, with patients informed consent and procedures approved by regional ethics committee (Ref. number: DNR 2011/358-31). Two cases of unilateral AFFs in two female patients were identified based on published diagnostic criteria [2,67], with age between 70-80 years old and around 10 years of continuous oral BPs treatment before the fractures. Both patients had intramedullary nailing fixation within a few weeks after the incomplete fracture was diagnosed. During surgery, a skin incision was made on the lateral thigh to expose the fracture site. A cylindrical bone biopsy (diameter = 8-15 mm) containing the full-thickness cortical bone across the fracture site was excised with chisel and drill saw [68]. The sample was fixed in 4% buffered formaldehyde and kept in 70% ethanol. For comparison, two age and gender-matched femoral fracture patients without BPs exposure or other baseline bone metabolic disorders except for osteoporosis were included in Shantou University Medical Center. The biopsies were obtained with the same manner as those for AFFs. Specimens from both groups were decalcified (4% formic acid), paraffin-embedded, and sectioned at 5 um thickness. For H&E staining of AFF sample, the procedure was indicated in the published article [68]. For immunofluorescence staining, sections were incubated with primary antibodies against CGRP, collagen 3 overnight. Then, the specimens were incubated with fluorescence-conjugated secondary antibodies for 1 hour and coversliped with DAPI (Pro-Long Gold antifade reagent, Thermo Fisher Scientific). The sample was imaged with fluorescence microscopy (Leica Q500MC, Leica). Antibodies used are summarized in Table S6.

Rats

All animal experimental studies were approved by Animal Experimentation Ethics Committee of the Chinese University of Hong Kong (CUHK) (Ref. number: 18-087-GRF) and performed in accordance with Cap. 340. Animals (Control of Experiments) Ordinance, Department of Health, Hong Kong SAR. Six months old female Sprague Dawley (SD) rats were obtained from the animal center of CUHK and housed on a 12-12-hour dark light cycle with free access to water and standard rodent diet. After arriving in the animal house, all rats were kept for 2 weeks to acclimate to the environment before commencement of the designed experiments.

Bisphosphonate Treatment

Zoledronate (ZOL), one of the most potent and popularly prescribed bisphosphonates, was purchased from Sigma-Aldrich (1724827-150MG), and dissolved in 0.9 % $NaCl_2$ to prepare an injection solution at a concentration of 0.2 mg/ml. For ovariectomy (OVX) rats, ZOL treatment was not initiated until osteoporosis was established three months after OVX. Then, ZOL was subcutaneously administrated for 3 or 6 months at a regimen of 0.3 mg/kg/week and 0.1 mg/kg/3 months, respectively. Control rats were administrated with an equal volume of saline for 3 or 6 months. For non-OVX rats, ZOL at a dose of 0.3 mg/kg/week was injected to 6-month-old female rats for 3 months. The dose of 0.3 mg/kg/week was used to experimentally study the potential side effects of BPs on a relatively short period of time, and also to mimic the clinical setting of using ZOL (5 mg/month/person) to treat cancers, while the lower dose (0.1 mg/kg/3 months) was to mimic the clinical anti-osteoporotic regimen (5 mg/year/person) [69–71]. All the treatment regimens have been demonstrated to be safe in terms of general health conditions of rats.

555 *Fabrication of Magnesium-containing Intramedullary Nail (Mg-IMN)*

556 Our previous study has validated the feasibility and efficacy of hybrid Mg-IMN to fix and promote

557 repair of rat osteoporotic fractures via releasing Mg ions to the peri-implant bone tissues [19]. In

558 the current study, the same hybrid implant was employed to fix fractures in rats with or without

559 ZOL treatment. In brief, pure Mg pins (99.99 wt.%), with a diameter and length of 0.8 mm and 10

560 mm, respectively, were purchased from Dongguan Eontec Co., Ltd, China. Hollow spinal needles

561 were purchased from Terumo, Japan. Eighteen interlacing holes, each with a diameter of 0.5 mm,

562 were drilled across the middle 1 cm of the needle, with 0.5 mm between each vent. The fabrication

563 was achieved by electric sparks burning at Ziyoujian company (Shenzhen, China). Then, the pure

564 Mg pin was inserted inside the hollow IMN to the site with vents, forming a hybrid Mg-containing

565 IMN system. This system was later used to fix fractures by positioning the vents at the level of

566 fracture line, and as a result allowed Mg ions effectively released into the surrounding tissues.

567

568 *Surgeries*

569 *Ovariectomy* General anaesthesia was achieved by intra-peritoneal injection of ketamine (75

570 mg/kg) in conjunction with xylazine (10 mg/kg). Abdomens of rats were shaved and sterilized

571 with 75% ethanol. Then, a 1.5 cm skin incision was made by using a surgical blade 1 cm above

572 the symphysis pubis along the central abdominal line. Surgical scissors and forceps were used to

573 separate abdominal muscles and fasciae, and to open the peritoneal cavity. Then, bilateral ovaries

574 were found and pulled out of the abdominal cavity followed by a resection. Ligation of the residual

575 tissues, including fallopian tubes, fat, and vessels, was performed with 5-0 silk suture for

576 hemostasis. After this, 5-0 Vicryl Plus sutures (Johnson & Johnson) were used to close the

577 abdominal wall via reapproximating wound edges of muscles and fasciae. Skin wounds were then

578   sutured by 5-0 silk sutures (Johnson & Johnson), and rats were recovered from anaesthesia under

579   warm condition (37°C) before returning to the animal house. Postoperatively, Temgesic (Schering-

580   Plough) at a dose of 0.05 mg/kg was subcutaneously administrated on three consecutive days for

581   the purpose of analgesia.

582

583   *Unilateral Closed Fracture* After 3 or 6 months of ZOL treatment, closed fracture of the right

584   femur was established using our published protocol [19]. Briefly, under anaesthesia with ketamine

585   (75 mg/kg) and xylazine (10 mg/kg), shaving of the right hind limb was performed from right knee

586   joint to the greater trochanter region, followed by sterilization using 75% ethanol. Then, a 5 mm

587   skin incision was cut along the medial parapatellar region to allow for dislocation of the patella

588   and exposure of intercondylar notch under a flexure position of the knee. Reaming of the medullary

589   cavity through intercondylar notch was performed using a 18G needle till it penetrated the cortex

590   of greater trochanter, followed by placing a thinner guiding pin into the reamed medullary cavity

591   and removal of the 18G needle. After this, the rat was placed supine with its femur supported with

592   anvils of a commercially available fracture apparatus introduced by Einhorn et al [72]. This

593   guillotine ramming system was driven by a dropping weight (500 g, 35 cm in height), subsequently

594   resulting in a transverse fracture of the pre-pinned right femoral diaphysis, which was further

595   confirmed by radiographs on anterior-posterior and lateral views. Fixation of fractures was

596   performed by using either normal IMN or Mg-IMN: (1) For those with IMN, a stainless-steel made

597   18G needle (Terumo, Japan) was inserted into the fractured bone with gradual removal of the

598   thinner guiding pin. Stabilization of the fracture gap during this process was paid particular

599   attention to prevent dislocation of the fracture line. After the needle penetrated proximal femoral

600   cortex, its tip was curved and hooked onto the greater trochanter to prevent the displacement of

601　the fixator into the knee joint. (2) For those with Mg-IMN, the spinal needle with drilled vents

602　was inserted into the fractured bone, instead of using 18G needle. The guiding pin was then

603　removed, followed by insertion of Mg pin through the canal of spinal needle to the sites with drilled

604　vents. The position of this Mg-IMN was adjusted with the help of radiograph to ensure the fracture

605　line was covered by vents. Then, the proximal ending of Mg-IMN was curved into a hook and

606　fixed onto greater trochanter. The knee joint capsule was closed with repositioning of patella to its

607　anatomic position with 5-0 Vicryl Plus suture (Johnson & Johnson), and the skin wound was

608　reapproximated by 5-0 silk suture (Johnson & Johnson). All the rats were recovered from aesthesia

609　under warm condition (37°C), and daily analgesics (Temgesic) at a dose of 0.05 mg/kg were given

610　for 3 days post-operationally.

611

612　***CGRP injection***

613　Daily percutaneous injection of CGRP (100 nM, 100 μl/rat/day) was performed to fracture gaps

614　of ZOL-pretreated rats for the first 14 days of fracture healing. The dose was chosen based on our

615　previous studies showing that a higher dose did not further promote bone repair in rats [19,46].

616　Decision for treating 14 days was made on the fact that CGRP has been proved to enhance fracture

617　healing at the early stages of fracture healing [19]. In brief, on day 1 post-fracture rats were sedated

618　under sevoflurane. CGRP (ab47101, Abcam) was dissolved into protein stabilizing cocktail

619　(Thermo Fisher Scientific) to achieve a working concentration of 100 nM. Then, 100 μl of CGRP

620　solution was percutaneously injected to tissues around the fracture site using a microinjection

621　syringe (NanoFil™, World Precision Instrument). Rats were recovered from anaesthesia, and

622　injection was performed on a daily basis for 14 consecutive days post-fracture.

623

In vivo Ramp1 knockdown using shRNA-adenovirus

624

Sequence of *Ramp1* shRNA was designed (Table S7) according to our published article [19]. Anti-*Ramp1* shRNA packed adenoviruses were generated by BioWit Technologies Ltd. (Shenzhen, China) using AdMAX packaging system (http://www.biowit.com/page-103-e.html), the efficacy of which has been proved in our published work. Three days before the fracture surgery, rats were put under general anaesthesia, and a hole was drilled at the lateral epicondyle of the right femur (the side to be fractured). Then, *Ramp1* shRNA packaging adenoviruses were injected into the medullary cavity (10 μl, with 10^9 pfu). Similarly, an equal number of adenoviruses were injected to periosteum of the femoral midshaft. For negative control, adenoviruses carrying scrambled sequence were injected to either bone marrow or periosteum. This gene expression knockdown strategy has been proved to be bio-effective *in vivo* for at least 8 weeks [47].

X-ray analysis

Post-operatively, rats were subjected to sequential radiographic imaging (UltraFocus DXA, Faxitron) to monitor fracture healing process using our established protocol [19]. Briefly, under anaesthesia rats were placed in a prone position to receive an exposure of 30 kv for 5 seconds. Radiographic healing was defined as bridging of the mineralized external callus on AP-view of X-rays and assessed by three independent orthopaedic surgeons blinded to the grouping information. A fracture was defined as radiographic bridging. Both callus width (CW) and callus area (CA) were digitalized and measured using ImageJ software by calculating the maximal width of the fracture callus and size of the radiopaque area of the callus, respectively. The calculation was repeated by three independent orthopaedic surgeons blinded to the grouping information, and the average score was used for statistics.

647 ***Micro-CT***

648 *Bone morphologic Analysis.* After euthanasia with overdose phenobarbital, soft tissues and

649 intramedullary fixators were carefully removed from the fractured femora, and the specimens were

650 placed in a sample tube (diameter of 38 mm) and scanned (μCT 40, Scanco Medical) using our

651 published protocol [19]. In brief, the spatial resolution was 16 μm, and scan range was 200 slides

652 (3 mm) distal and 200 slides (3 mm) proximal to the fracture line. Region of interests was selected

653 on 2D images. Standardized threshold of mineralized bone was set to be >165. For 3D

654 reconstruction, a low-pass Gaussian filter was selected (Sigma = 1.2, Support = 2). Data generated

655 from 400 slices of 2D pictures was used for statistical analysis of morphologic parameter,

656 including bone volume (BV), total volume (TV), BV/TV, bone mineral content of BV (BMC of

657 BV), bone mineral content of TV (BMC of TV), bone mineral density of BV (BMD of BV), and

658 bone mineral density of TV (BMD of TV).

659

660 *Angiography.* Angiography was performed to assess neovascularization of fractured bone using

661 our established protocol [73]. In brief, rats were put into deep anaesthesia with overdose

662 phenobarbital, followed by thoracotomy to expose the heart. The right axillary vein was cut to

663 drainage blood. A catheter was inserted into the left ventricle to allow for perfusion of heparinized

664 phosphate buffered saline (PBS) with 0.2 % heparin sodium salt for a total volume of 50 ml,

665 followed by 20 ml 4% buffered paraformaldehyde (PFA). After this, lead chromate and lead

666 sulfate-contained radiopaque silicone rubber compound (Microfil MV-122, Flow Tech) were

667 administrated slowly via the left heart, and a total amount of 30 ml Microfil was used for each rat.

668 After sealing of right heart slit, the rats were stored at 4°C for 24 hours to allow for polymerization,

669 followed by fixation of the specimen in 10% buffered formalin for two days. The fractured bones

670 were then decalcified in 9% formic acid for 4 weeks, and used for CT scanning (μCT 40, Scanco

671 Medical) at a spatial resolution of 16 μm. Region of interest (ROI) was set on 2D image with a

672 range of 400 slides centred on the fracture gap. Three-dimensional reconstruction of the vessels

673 was then completed with a threshold of 100.

674

675 *Histological Analysis*

676 Bone samples were fixed (4% buffered formalin for 2 days), decalcified (4% formic acid for 4

677 weeks), and dehydrated by series ethanol and xylene. Paraffin embedding and longitudinal section

678 at a thickness of 6 μm (Leica microtome RM2255, Leica) were then performed. The samples were

679 subjected to hematoxylin and eosin (H&E) and Safranin O/Fast Green staining using our

680 established protocol [19]. For immunohistochemistry (IHC) staining, the sections were

681 deparaffinized and rehydrated before quenching of endogenous peroxide by 3% hydrogen peroxide

682 for 20 minutes. Antigen retrieval was achieved by immersing the slides into citric acid buffer at a

683 temperature of 95°C for 20 minutes. After blocking with solution containing 1% bovine serum

684 albumin (BSA, Thermo Fisher Scientific) and 5% fetal bovine serum (FBS, Thermo Fisher

685 Scientific) for 1 hour, the samples were incubated at 4°C overnight with primary antibodies for

686 Cd3, Cd14, Cd19, Cd68, alpha-smooth muscle actin (α-SMA), calcitonin gene-related peptide

687 (CGRP), receptor activity-modifying protein 1 (Ramp1), calcitonin receptor-like receptor (Crlr).

688 For negative control, slides were incubated with solutions without primary antibody. Subsequently,

689 slides were washed 3 times by PBS and incubated for 1 hour at room temperature with goat anti-

690 rabbit secondary antibody conjugated to horseradish peroxidase (HRP). The samples were then

691 incubated with DAB/HRP system (DAB Quanto Chromogen and Substrate, Thermo Fisher

692 Scientific) for 5 minutes to detect immunoactivities, and counterstained with hematoxylin before

693 being cover-slipped. Specimens were viewed under light microscopy (Leica Q500MC, Leica). For

694 immunofluorescence staining, tissue slides were incubated with primary antibodies for Cd10,

695 Cd26, CGRP, and collagen 3 overnight, followed by treatment with specific fluorescence-

696 conjugated secondary antibodies for one hour. Rinsed sections were coversliped with DAPI (Pro-

697 Long Gold antifade reagent, Thermo Fisher Scientific), the tissues were imaged under fluorescence

698 microscopy (Leica Q500MC, Leica). Antibodies and reagent used were summarized in Table S8.

699

700 ***Harvest of dorsal root ganglion (DRG)***

701 For those used for immunofluorescent staining for CGRP, fractured rats were maintained under

702 anesthesia (ketamine, 75 mg/kg; xylazine, 10 mg/kg), trans-cardia perfused with 4% PFA before

703 dissection of right L4 DRG. For those used for *in vitro* culturing, 6-month-old healthy female rats

704 were euthanized with overdose phenobarbital without perfusion, and fresh L4 DRGs from both

705 sides were harvested and cultured. In brief, after laminectomy, spinal cord was removed to better

706 expose cauda equina, dorsal nerve root, and the dorsal root ganglion. L4 DRG was identified

707 according to its morphology (biggest) and physical location (intervertebral foramen). The DRG

708 was then resected and subjected to further procedures.

709

710 ***Staining for CGRP in DRG***

711 DRG from PFA-perfused animal was post-fixed in PFA for 24 hours, dehydrated in 30% sucrose

712 for 2 days, and embedded in optimal cutting temperature compound. Frozen sections were cut at a

713 thickness of 20 μm and adjusted for further immunofluorescence staining. Slides were blocked for

714 1 hour using 5% FBS with 0.001% Trion X-100 in PBS, followed by incubation with rabbit anti-

715 CGRP primary antibody (Abcam) over night. Then, the specimens were incubated with

716 fluorescence-conjugated secondary antibody (Goat anti-rabbit, Alexa Fluor 488, Thermo Fisher

717 Scientific) for 1 hour, before being coversliped with DAPI (Pro-Long Gold antifade reagent,

718 Thermo Fisher Scientific). The sample was imaged with fluorescence microscopy (Leica Q500MC,

719 Leica). Antibodies used was summarized in Table S9.

720

Culture of DRG

722 A total amount of 15 fresh DRGs were harvested from healthy rats, and equally distributed into 15

723 centrifuge tubes (1.5 ml, sterilized, Becton Dickinson), each of which contains 1 DRG in 1ml

724 complete alpha-MEM (10% FBS, 1% PSN, all from Thermo Fisher Scientific). After culturing in

725 humidified incubators (37°C, 5% CO2) for 24 hours, the medium was changed to complete alpha-

726 MEM containing zoledronate and/or $MgCl_2$ at different concentrations, according to which five

727 groups were designed: 1) control (basal complete alpha-MEM); 2) zoledronate low dose (ZL, ZOL

728 at 500 nM); 3) zoledronate high dose (ZH, ZOL at 5 μM); 4) zoledronate low dose + $MgCl_2$ (ZLM,

729 Mg at 1 mM); 5) zoledronate high dose + $MgCl_2$ (ZHM, Mg at 1mM). Samples were harvested for

730 extraction of RNA after 2 days of culture. For total RNA extraction, DRGs were immersed into

731 RNAiso Plus (Takara Bio) solution and snap frozen into liquid nitrogen before being transferred

732 to -80 degrees Celcius storing condition. Tissues were then grinded to extract total RNA, which

733 were then subjected to reverse transcription polymerase chain reaction (RT-PCR) to measure gene

734 expression level of CGRP (Table 10).

735

Isolation and culture of primary bone marrow stem cells (BMSCs)

737 Collection of primary BMSCs was performed according to published protocol, which has proven

738 to yield a high successful rate and stem cell purity [74]. For isolation of BMSCs from intact bone,

739 the femora were harvested under sterile conditions and cut half in the middle by scissors. Then

740 bone marrow cells were flushed out with 10 ml complete alpha-MEM (10% FBS and 1% PSN)

741 using a syringe with a 21G needle inserted into the medullary cavity. For isolation of BMSCs from

742 fractured bone fixed with IMN or Mg-IMN, fixators were carefully removed from the fractured

743 femora before flushing the medullary cavity to obtain bone marrow cells. Flushing was repeated

744 for 3-5 times till the bone marrow became pale. The collected bone marrow cells suspension

745 containing fat and debris were then directly plated in 10 cm cell culture dish (Becton Dickinson)

746 without filtering or washing. The plate was stored in the incubator at 37°C with 5% CO2 before

747 removal of nonadherent cells on the third day. Afterwards, the cells were kept in the incubator

748 (37°C with 5% CO2) with medium being changed every 3 days. Subculture was performed when

749 the spindle cells reached 80% confluence. Cells at passages 2-4 were used for further tests.

750

751 ***Osteogenic differentiation of BMSCs***

752 Osteogenic induction medium (OIM) was prepared according to our published protocol [19].

753 Complete high glucose DMEM (10% FBS, 1% PSN, Thermo Fisher Scientific) was supplemented

754 with dexamethasone (100 nM), vitamin C (50 μM), beta-glycerophosphate (20 mM), and sodium

755 pyruvate (110 mg/L) (all chemicals were from Sigma-Aldrich). Cells at passage 3-5 were seeded

756 at a density of 4×10^3 cells/cm^2 in 6-well plates with complete alpha-MEM, which was changed

757 every 3 days. When cells reached 80% confluence, osteogenic induction was started with the

758 replacement of complete alpha-MEM with OIM, which was then changed every 3 days. At day 14

759 or 21, the cells were subjected to Alizarin Red S staining (1%, Sigma-Aldrich) and imaged by light

760 microscopy. In addition, total RNA was extracted from each well via adding 500 μl of RNAiso

761   Plus (Takara Bio) solution following the protocol provided by the manufacturer. For RT-PCR,

762   target genes were selected to be *Osterix*, *Runx2*, *Bmp2*, *Spp1* (*Osteopontin*), and *Alp* (Table S10).

763

764   ***Adipogenic differentiation***

765   Adipogenic induction medium (AIM) was used in accordance with our published protocol (132):

766   complete high glucose DMEM (10% FBS, 1% PSN, Thermo Fisher Scientific) was supplemented

767   with dexamethasone (500 nM), indomethacin (50 μM), isobutylmethylxanthine (0.5 mM), and

768   insulin (10 μg/ml) (all chemicals were from Sigma-Aldrich). After cells reached 80% confluence

769   in 6-well plate, alpha-MEM was replaced with AIM with the medium changed every 3 days. After

770   9 days of induction, the cells were fixed (4% PFA) and stained with Oil Red O (0.5%, Sigma-

771   Aldrich) for 15 minutes. The adipocytes with intracellular droplet were imaged under light

772   microscopy. Besides, total RNA was extracted (RNAiso Plus, Takara Bio) from each well for RT-

773   PCR of adipogenic genes, including *Pparg*, *cebpa*, and *adiponectin* (Table S11).

774

775   ***Fibrogenic differentiation***

776   *BMSCs isolated from the fractured rats.* According to published protocol [75,76], BMSCs at

777   passage 3-5 were seeded at 12-well plate (4×10^3 cells/cm^2). When the cells reached 80%

778   confluence, basal culture medium (complete alpha-MEM with 10% FBS and 1% PSN) was

779   replaced with fibrogenic induction medium (FIM), which contained fibroblast growth factor-basic

780   (bFGF, 20 ng/ml) and epidermal growth factor (EGF, 20 ng/ml) in complete HG DMEM medium

781   (10% FBS, 1% PSN, 110 mg/L sodium pyruvate) (all reagents were purchased from Thermo Fisher

782   Scientific). Fibrogenic induction medium was changed every 3 days. After 11 days of induction,

783   cells were subjected to immunocytochemistry staining or analysis for gene expression. For

784 immunocytochemistry staining, cells were fixed with 4% PFA, incubated with primary antibodies

785 for CGRP, collagen 3, and Cd10 overnight. Then, cells were treated with fluorescence-conjugated

786 secondary antibodies for one hour and coversliped with DAPI. The sample was imaged with

787 fluorescence microscopy (Leica Q500MC, Leica). Antibodies used was summarized in Table S12.

788 For RNA expression, RNAs were extracted using RNAiso Plus (Takara Bio) for RT-PCR of

789 fibrogenic markers, including transforming growth factor beta 1 (TGF-beta1), collagen Ia (Col1a),

790 S100a4, heat shock protein 47 (Hsp47). Primers of these markers were listed in Table S13.

791

792 *In vitro treatment of BMSCs with ZOL, Mg ions, and CGRP.* BMSCs from femora of 9-month-old

793 healthy female rats were harvested and seeded in 12-well plates. After the cells reached 80%

794 confluence, culture medium was changed to basal FIM or FIM added with 1) low dose ZOL (500

795 nM); 2) high dose ZOL (5 μM); 3) $MgCl_2$ (10 mM); 4) CGRP (10 nM); 5) low dose ZOL + $MgCl_2$;

796 6) high dose ZOL + $MgCl_2$; 7) low dose ZOL + CGRP; 8) low dose ZOL + CGRP (ZOL and

797 $MgCl_2$ were from Sigma, CGRP was from Abcam). Medium was changed every 3 days. On day

798 11, cells were subjected for RT-PCR of fibrogenic markers listed in Table S13.

799

Isolation and culturing of fracture callus cells

801 Post-operationally, fracture callus cells (FCCs) were harvested following a protocol similar to ones

802 used for collections of periosteum or tendon derived stem cells [19,77]. In brief, rats were

803 sacrificed with cervical dislocation under general anesthesia using ketamine (75 mg/kg) and

804 xylazine (10 mg/kg). Immediately after this, the fractured femora were collected and transferred

805 into sterilized PBS solution. In biosafety cabinet, the fixator (IMN or Mg-IMN) was pulled out,

806 and muscles were carefully resected without dissociating superficial connective tissue (containing

807 periosteum) from the femur. Then, soft tissues within the fracture gap together with periosteum (5

808 mm distal, and 5 mm proximal to the fracture line) were scraped off using a surgical blade, cut

809 into 1 mm3 pieces, and transferred to a sterilized 15 ml centrifuge tube containing 3 ml LG DMEM

810 supplemented with 10% FBS and type I collagenase (1 mg/ml) (all reagents from Thermo Fisher).

811 The specimen was digested in a 37°C incubator with 5% CO_2 overnight, and the released cells

812 were obtained via passing through a 70 μm cell strainer (Becton Dickinson). The cells were

813 centrifuged (500 × g for 8 minutes) and resuspended in complete alpha-MEM (with 10% FBS, 1%

814 PSN). Around 100,000- 200,000 cells were harvested from each animal and cells from four rats

815 per group were pooled for further analysis. For flow cytometry, 10,000 cells from each group were

816 analyzed. For mRNA-seq, the pooled cells were seeded on a 10 cm cell culture dish (Becton

817 Dickinson) before digestion for library preparation.

818

819 *Flow cytometry of fracture callus cells*

820 The proportions of fibroblasts, which are Cd26/S100a4 double-positive, and CGRP-positive stem

821 cells, which are Cd105/CGRP double-positive, in FCCs were identified using flow cytometry

822 according to established protocol [19,78]. The isolated primary FCCs were centrifuged (500 × g

823 for 8 minutes) and washed twice by PBS. Then, the cells were resuspended into 200 μl single-cell

824 suspension in PBS (5×10^5/ml) containing 0.04% BSA and primary antibodies against CGRP,

825 Cd105, S100a4, and/or Cd26 (Table S14). Then, the cells were incubated at 37°C for 1 hour,

826 washed 3 times with PBS, and subsequently incubated with secondary antibodies against mouse

827 and/or rabbit for 30 minutes (Table S14). In the meantime, FCCs without antibody staining was

828 set as control, and isotype antibodies control was also set. After washing out primary antibodies 3

829 times with PBS and resuspending cells in complete alpha-MEM to form single cell suspensions,

830   flow cytometry was performed on BD FACSAria™ Fusion Cell Sorter. Singlet cell populations

831   were gated, and thresholds for FITC-A (488 nm) and PE-A (594 nm) were set. Data were acquired

832   from a total amount of 10,000 cells/sample, and further analyzed using FlowJo software (Tree

833   Star).

834

835   ***Reverse transcription and RT-PCR***

836   Total RNA was harvested from DRG or cells. After confirmation of the RNA concentration using

837   NanoDrop 2000 Spectrophotometers (Thermo Fisher Scientific), reverse transcription was

838   performed using PrimeScript RT Reagent Kit (Takara Bio) to obtain 20 μl of cDNA from 500 ng

839   of RNA per sample. Real-time PCR was then applied using SYBR Premix Ex Taq (10 μl reaction

840   system in 384-well plates, Takara Bio) with ABI 7900HT real-time PCR system (Applied

841   Biosystems). Relative mRNA expression level ($2^{-\Delta CT}$) was normalized using beta-action as a

842   housekeeping gene and presented as fold changes over control.

843

844   ***Single-cell RNA sequencing (scRNA-seq)***

845   After isolation of FCCs from fracture callus tissues at week 4 and 12 post-fracture, the cells from

846   4 rats in each group were pooled together and subjected to single-cell RNA sequencing (scRNA-

847   seq) using 10X Genomics Chromium platform (BGI, Shenzhen). Reverse transcription was

848   performed to construct single-cell libraries, followed by paired-end Illumina sequencing (HiSeq

849   4000, one lane) which yielded ~ 340 million reads per sample. Reads were than mapped to rat

850   reference genome (STAR aligner v2.5.1b), with an average of 3299 ± 46 (mean ± s.e.m.) genes

851   detected in each sample. For quality control, cells with total number of expressed genes < 500,

852　genes expressed < 5 cells, and mitochondrial DNA > 20% were excluded for downstream analysis

853　using RStudio software (R version 3.6.2).

854

855　### *Dimension reduction and cell clustering*

856　Seurat 3.1.5 R package was applied to cluster FCCs. Data from each group at each group were

857　analyzed separately or merged for integrated analysis using *FindIntegrationAnchors* function.

858　Reads information were normalized by *LogNormalize* function to limit cell-to-cell variation in

859　sequencing depth. Then, highly variable genes were located by using *FindVariableFeatures*

860　function, followed by principal component analysis (PCA) and selection of top 30 components

861　arranged on elbow plot to perform clustering. The outcome was visualized on 2D image of t-

862　distributed stochastic neighbor embedding (t-SNE). *FindAllMarkers* function was then used to

863　discover differentially expressed genes (DEGs) for each cluster, and the fibroblastic nature of the

864　clusters was confirmed based on expression of common fibroblasts genes [41,79]. Gene Ontology

865　(GO) analysis associated with 'biological process' was conducted based on DEGs of each cluster

866　using 'gsfisher' R package [79].

867

868　### *Monocle analysis*

869　Monocle 2.14 was used to illustrate the developmental relationship between different clusters.

870　Briefly, the scRNA-seq data with clustering information obtained by Seurat was input into a

871　Monocle project in R, while raw read counts were used instead of normalized ones. Then, cluster

872　information identified by Seurat was used to perform dimension reduction with 'DDRTree'

873　method, and the developmental trajectory was visualized on 2D images. The DEGs on pseudo-

874　time trajectory was also identified and visualized using '~sm.ns (Pseudo-time)'.

875

Statistical Analysis

GraphPad Prism software (GraphPad Software) was used to perform the statistical analysis for quantitative data. For multiple time point comparison, one-way (for single group) or two-way (for two groups or multiple groups) analysis of variance (ANOVA) was utilized for comparison, with further testing the defined difference using relevant *post-hoc* test(s). *t*-test was only used to compare between-group differences at a single time point for the current study if only single time is used for defined variable(s). Significance level was set at $p < 0.05$ (two-tailed).

883

884

885

886

887

888

889

890

891

Author contributions: L.Q., N.Z., J.X., and R.O. were responsible for conceptualization, experimental design, performed experiments, data collection and analysis, visualization, and writing and proofread. Y.R., L.C., and X.W. established methodologies, validation. R.Z. and Q.X. performed experiments and assisted with data analysis. N.T., T.O., and J.S. provided clinical samples and storage. H.Y. and J.W. conducted μCT scanning, perfusion for angiography.

Competing interests: Authors declare no competing interests.

Materials & Correspondence: mRNA sequencing data were deposited in GEO under accession code GSE185988. Correspondence regarding to experiments, data, and material should be addressed to N.Z. and J.X.

References

[1] E.S. Siris, M.K. Pasquale, Y. Wang, N.B. Watts, J. Bone Miner. Res. 26 (2011) 3–11.

[2] E. Shane, D. Burr, P.R. Ebeling, B. Abrahamsen, R.A. Adler, T.D. Brown, A.M. Cheung, F. Cosman, J.R. Curtis, R. Dell, D. Dempster, T.A. Einhorn, H.K. Genant, P. Geusens, K. Klaushofer, K. Koval, J.M. Lane, F. McKiernan, R. McKinney, A. Ng, J. Nieves, R. O'Keefe, S. Papapoulos, H.T. Sen, M.C.H. van der Meulen, R.S. Weinstein, M. Whyte, American Society for Bone and Mineral Research, J. Bone Miner. Res. 25 (2010) 2267–2294.

[3] N. Zheng, N. Tang, L. Qin, Journal of Orthopaedic Translation 7 (2016) 7–22.

[4] R.M. Dell, A.L. Adams, D.F. Greene, T.T. Funahashi, S.L. Silverman, E.O. Eisemon, H. Zhou, R.J. Burchette, S.M. Ott, J. Bone Miner. Res. 27 (2012) 2544–2550.

[5] J. Schilcher, V. Koeppen, P. Aspenberg, K. Michaëlsson, New England Journal of Medicine 371 (2014) 974–976.

[6] K.-J. Lee, J.J. Yoo, K.-J. Oh, J.-H. Yoo, K.H. Rhyu, K.W. Nam, D.-H. Suh, Injury 48 (2017) 941–945.

[7] Y.S. Lai, J.Y.M. Chau, S.B. Woo, C. Fang, T.W. Lau, F. Leung, Geriatr Orthop Surg Rehabil 10 (2019) 2151459319864736.

[8] S.-J. Lim, I. Yeo, P.-W. Yoon, J.J. Yoo, K.-H. Rhyu, S.-B. Han, W.-S. Lee, J.-H. Song, B.-W. Min, Y.-S. Park, Osteoporos Int 29 (2018) 2427–2435.

[9] M.T. Nagy, G. Pydisetty, T.A. Kwaees, K. Saldanha, Injury 52 (2021) 582–588.

[10] Y.-T. Li, H.-F. Cai, Z.-L. Zhang, Osteoporos Int 26 (2014) 431–441.

[11] M.M. McDonald, A. Morse, L. Peacock, K. Mikulec, A. Schindeler, D.G. Little, J. Orthop. Res. 29 (2011) 726–733.

[12] H.P. Bögl, P. Aspenberg, J. Schilcher, Osteoporos Int (2017) 1–6.

[13] R.A. Lindtner, A.N. Tiaden, K. Genelin, H.L. Ebner, C. Manzl, M. Klawitter, I. Sitte, B. von Rechenberg, M. Blauth, P.J. Richards, Osteoporos Int 25 (2013) 1151–1161.

[14] S.G. Grässel, Arthritis Res. Ther. 16 (2014) 485.

[15] F. Hara-Irie, N. Amizuka, H. Ozawa, Bone 18 (1996) 29–39.

[16] M. Hukkanen, Y.T. Konttinen, S. Santavirta, P. Paavolainen, X.-H. Gu, G. Terenghi, J.M. Polak, Neuroscience 54 (1993) 969–979.

[17] M. Aoki, K. Tamai, K. Saotome, International Orthopaedics 18 (1994) 317–324.

[18] T. Schinke, S. Liese, M. Priemel, M. Haberland, A.F. Schilling, P. Catala-Lehnen, D. Blicharski, J.M. Rueger, R.F. Gagel, R.B. Emeson, M. Amling, Journal of Bone and Mineral Research 19 (2004) 2049–2056.

[19] Y. Zhang, J. Xu, Y.C. Ruan, M.K. Yu, M. O'Laughlin, H. Wise, D. Chen, L. Tian, D. Shi, J. Wang, S. Chen, J.Q. Feng, D.H.K. Chow, X. Xie, L. Zheng, L. Huang, S. Huang, K. Leung, N. Lu, L. Zhao, H. Li, D. Zhao, X. Guo, K. Chan, F. Witte, H.C. Chan, Y. Zheng, L. Qin, Nat Med 22 (2016) 1160–1169.

[20] J.M. Brazill, A.T. Beeve, C.S. Craft, J.J. Ivanusic, E.L. Scheller, Journal of Bone and Mineral Research 34 (2019) 1393–1406.

[21] S. Zheng, W. Li, M. Xu, X. Bai, Z. Zhou, J. Han, J.Y.-J. Shyy, X. Wang, American Journal of Physiology - Cell Physiology 299 (2010) C1485–C1492.

[22] S. Zhu, J. Zhu, G. Zhen, Y. Hu, S. An, Y. Li, Q. Zheng, Z. Chen, Y. Yang, M. Wan, R.L. Skolasky, Y. Cao, T. Wu, B. Gao, M. Yang, M. Gao, J. Kuliwaba, S. Ni, L. Wang, C. Wu, D. Findlay, H.K. Eltzschig, H.W. Ouyang, J. Crane, F.-Q. Zhou, Y. Guan, X. Dong, X. Cao, J Clin Invest 129 (2019) 1076–1093.

[23] S. Orita, S. Ohtori, T. Koshi, M. Yamashita, K. Yamauchi, G. Inoue, M. Suzuki, Y. Eguchi, H. Kamoda, G. Arai, T. Ishikawa, M. Miyagi, N. Ochiai, S. Kishida, M. Takaso, Y. Aoki, T. Toyone, K. Takahashi, Spine 35 (2010) 1974–1982.

[24] T. Nakagawa, H. Wakabayashi, Y. Naito, S. Kato, T. Iino, A. Sudo, Ann Rheum Dis 74 (2015) 535–535.

[25] Y.Y. Yu, S. Lieu, D. Hu, T. Miclau, C. Colnot, PLoS ONE 7 (2012) e31771.

[26] P. Fournier, S. Boissier, S. Filleur, J. Guglielmi, F. Cabon, M. Colombel, P. Clézardin, Cancer Res 62 (2002) 6538–6544.

[27] A.P. Kusumbe, S.K. Ramasamy, R.H. Adams, Nature 507 (2014) 323–328.

[28] S.K. Ramasamy, A.P. Kusumbe, L. Wang, R.H. Adams, Nature 507 (2014) 376–380.

[29] H.-S. Han, I. Jun, H.-K. Seok, K.-S. Lee, K. Lee, F. Witte, D. Mantovani, Y.-C. Kim, S. Glyn-Jones, J.R. Edwards, Advanced Science 7 (2020) 2000800.

[30] B.J. Edwards, M. Sun, D.P. West, M. Guindani, Y.H. Lin, H. Lu, M. Hu, C. Barcenas, J. Bird, C. Feng, S. Saraykar, D. Tripathy, G.N. Hortobagyi, R. Gagel, W.A. Murphy, Journal of Bone and Mineral Research 31 (2016) 1569–1576.

[31] E. Gómez-Barrena, P. Rosset, D. Lozano, J. Stanovici, C. Ermthaller, F. Gerbhard, Bone 70 (2015) 93–101.

[32] F. von Knoch, C. Jaquiery, M. Kowalsky, S. Schaeren, C. Alabre, I. Martin, H.E. Rubash, A.S. Shanbhag, Biomaterials 26 (2005) 6941–6949.

[33] S. Su, J. Chen, H. Yao, J. Liu, S. Yu, L. Lao, M. Wang, M. Luo, Y. Xing, F. Chen, D. Huang, J. Zhao, L. Yang, D. Liao, F. Su, M. Li, Q. Liu, E. Song, Cell 172 (2018) 841-856.e16.

[34] M. Panagiotis, Injury 36 (2005) S30–S37.

[35] Y. Rinkevich, G.G. Walmsley, M.S. Hu, Z.N. Maan, A.M. Newman, M. Drukker, M. Januszyk, G.W. Krampitz, G.C. Gurtner, H.P. Lorenz, I.L. Weissman, M.T. Longaker, Science 348 (2015).

[36] K. Kaji, H. Yoshiji, Y. Ikenaka, R. Noguchi, Y. Aihara, A. Douhara, K. Moriya, H. Kawaratani, Y. Shirai, J. Yoshii, K. Yanase, M. Kitade, T. Namisaki, H. Fukui, J Gastroenterol 49 (2014) 481–491.

[37] H.S. Min, J.E. Kim, M.H. Lee, H.K. Song, Y.S. Kang, M.J. Lee, J.E. Lee, H.W. Kim, J.J. Cha, Y.Y. Chung, Y.Y. Hyun, J.Y. Han, D.R. Cha, Lab Invest 94 (2014) 598–607.

[38] G. Luo, P. Ducy, M.D. McKee, G.J. Pinero, E. Loyer, R.R. Behringer, G. Karsenty, Nature 386 (1997) 78–81.

[39] E.G. Frolova, N. Sopko, L. Blech, Z.B. Popović, J. Li, A. Vasanji, C. Drumm, I. Krukovets, M.K. Jain, M.S. Penn, E.F. Plow, O.I. Stenina, The FASEB Journal 26 (2012) 2363–2373.

[40] S. Unger, M.W. Górna, A. Le Béchec, S. Do Vale-Pereira, M.F. Bedeschi, S. Geiberger, G. Grigelioniene, E. Horemuzova, F. Lalatta, E. Lausch, C. Magnani, S. Nampoothiri, G. Nishimura, D. Petrella, F. Rojas-Ringeling, A. Utsunomiya, B. Zabel, S. Pradervand, K. Harshman, B. Campos-Xavier, L. Bonafé, G. Superti-Furga, B. Stevenson, A. Superti-Furga, The American Journal of Human Genetics 92 (2013) 990–995.

[41] C.F. Guerrero-Juarez, P.H. Dedhia, S. Jin, R. Ruiz-Vega, D. Ma, Y. Liu, K. Yamaga, O. Shestova, D.L. Gay, Z. Yang, K. Kessenbrock, Q. Nie, W.S. Pear, G. Cotsarelis, M.V. Plikus, Nature Communications 10 (2019) 650.

[42] A.C. Ochoa, A.H. Zea, C. Hernandez, P.C. Rodriguez, Clin Cancer Res 13 (2007) 721s–726s.

[43] D.N. Xanthos, J. Sandkühler, Nature Reviews Neuroscience 15 (2014) 43–53.

1003 [44] P. De Coppi, G. Bartsch Jr, M.M. Siddiqui, T. Xu, C.C. Santos, L. Perin, G. Mostoslavsky,
1004   A.C. Serre, E.Y. Snyder, J.J. Yoo, M.E. Furth, S. Soker, A. Atala, Nature Biotechnology 25
1005   (2007) 100–106.

1006 [45] D. Yu, F. Liu, M. Liu, X. Zhao, X. Wang, Y. Li, Y. Mao, Z. Zhu, PLOS ONE 8 (2013)
1007   e77824.

1008 [46] D.J. MI, D.J. Xu, D.H. Yao, D.X. Li, D.W. Tong, M.Y. Li, D.B. Dai, D.X. He, D.D.H.K.
1009   Chow, P.G. Li, P.K.O. Lui, P.J. Zhao, P.L. Qin, Https://Home.Liebertpub.Com/Tea (2020).

1010 [47] E. Wagner, K. Zatloukal, M. Cotten, H. Kirlappos, K. Mechtler, D.T. Curiel, M.L. Birnstiel,
1011   PNAS 89 (1992) 6099–6103.

1012 [48] L. Wang, R.J. Tower, A. Chandra, L. Yao, W. Tong, Z. Xiong, K. Tang, Y. Zhang, X.S. Liu,
1013   J.D. Boerckel, X. Guo, J. Ahn, L. Qin, Journal of Bone and Mineral Research 34 (2019) 520–
1014   532.

1015 [49] A. Julien, A. Kanagalingam, E. Martínez-Sarrà, J. Megret, M. Luka, M. Ménager, F. Relaix,
1016   C. Colnot, Nat Commun 12 (2021) 2860.

1017 [50] E. Gibon, L.Y. Lu, K. Nathan, S.B. Goodman, Journal of Orthopaedic Translation 10 (2017)
1018   28–35.

1019 [51] H. Wei, Y. Xu, Y. Wang, L. Xu, C. Mo, L. Li, B. Shen, Y. Sun, P. Cheng, L. Yang, Y. Pang,
1020   A. Qin, Y. Cao, S.J. Morrison, R. Yue, Cell Reports 33 (2020) 108252.

1021 [52] S. Debnath, A.R. Yallowitz, J. McCormick, S. Lalani, T. Zhang, R. Xu, N. Li, Y. Liu, Y.S.
1022   Yang, M. Eiseman, J.-H. Shim, M. Hameed, J.H. Healey, M.P. Bostrom, D.A. Landau, M.B.
1023   Greenblatt, Nature 562 (2018) 133.

1024 [53] C. Colnot, Journal of Bone and Mineral Research 24 (2009) 274–282.

1025 [54] X. Zhang, C. Xie, A.S. Lin, H. Ito, H. Awad, J.R. Lieberman, P.T. Rubery, E.M. Schwarz,
1026   R.J. O'Keefe, R.E. Guldberg, Journal of Bone and Mineral Research 20 (2005) 2124–2137.

1027 [55] X.-W. Li, X.-H. Li, J. Du, D. Li, Y.-J. Li, C.-P. Hu, Can. J. Physiol. Pharmacol. 94 (2016)
1028   1315–1324.

1029 [56] H.-X. Dang, J. Li, C. Liu, Y. Fu, F. Zhou, L. Tang, L. Li, F. Xu, International Journal of
1030   Molecular Medicine 40 (2017) 209–216.

1031 [57] P. Gasse, C. Mary, I. Guenon, N. Noulin, S. Charron, S. Schnyder-Candrian, B. Schnyder, S.
1032   Akira, V.F.J. Quesniaux, V. Lagente, B. Ryffel, I. Couillin, J Clin Invest 117 (2007) 3786–
1033   3799.

[58] J.-F. Xu, G.R. Washko, K. Nakahira, H. Hatabu, A.S. Patel, I.E. Fernandez, M. Nishino, Y. Okajima, T. Yamashiro, J.C. Ross, R. San José Estépar, A.A. Diaz, H.-P. Li, J.-M. Qu, B.E. Himes, C.E. Come, K. D'Aco, F.J. Martinez, M.K. Han, D.A. Lynch, J.D. Crapo, D. Morse, S.W. Ryter, E.K. Silverman, I.O. Rosas, A.M.K. Choi, G.M. Hunninghake, Am J Respir Crit Care Med 185 (2012) 547–556.

[59] J. Morry, W. Ngamcherdtrakul, S. Gu, S.M. Goodyear, D.J. Castro, M.M. Reda, T. Sangvanich, W. Yantasee, Biomaterials 66 (2015) 41–52.

[60] X.-Y. Ge, L.-Q. Yang, Y. Jiang, W.-W. Yang, J. Fu, S.-L. Li, PLOS ONE 9 (2014) e101207.

[61] N. Hagelauer, A.M. Pabst, T. Ziebart, H. Ulbrich, C. Walter, Clin Oral Invest 19 (2015) 139–148.

[62] T.-W. Tai, C.-Y. Chen, F.-C. Su, Y.-K. Tu, T.-T. Tsai, C.-F. Lin, I.-M. Jou, Sci Rep 7 (2017) 1–12.

[63] Q. Zhang, W. Yu, S. Lee, Q. Xu, A. Naji, A.D. Le, Journal of Bone and Mineral Research 30 (2015) 2300–2312.

[64] P. Lesclous, S. Abi Najm, J.-P. Carrel, B. Baroukh, T. Lombardi, J.-P. Willi, R. Rizzoli, J.-L. Saffar, J. Samson, Bone 45 (2009) 843–852.

[65] K. Xie, L. Wang, Y. Guo, S. Zhao, Y. Yang, D. Dong, W. Ding, K. Dai, W. Gong, G. Yuan, Y. Hao, Journal of Orthopaedic Translation 27 (2021) 96–100.

[66] J.-L. Wang, J.-K. Xu, C. Hopkins, D.H.-K. Chow, L. Qin, Advanced Science 7 (2020) 1902443.

[67] J. Schilcher, V. Koeppen, J. Ranstam, R. Skripitz, K. Michaëlsson, P. Aspenberg, Bone 52 (2013) 389–392.

[68] J. Schilcher, O. Sandberg, H. Isaksson, P. Aspenberg, Acta Orthop 85 (2014) 280–286.

[69] J. Yamashita, K. Koi, D.-Y. Yang, L.K. McCauley, Clin Cancer Res 17 (2011) 1405–1414.

[70] N. Amanat, M. McDonald, C. Godfrey, L. Bilston, D. Little, J. Bone Miner. Res. 22 (2007) 867–876.

[71] M.M. McDonald, S. Dulai, C. Godfrey, N. Amanat, T. Sztynda, D.G. Little, Bone 43 (2008) 653–662.

[72] F. Bonnarens, T.A. Einhorn, Journal of Orthopaedic Research 2 (1984) 97–101.

[73] S. Chen, L. Zheng, X. Xie, X. Wang, Y. Lai, S. Chen, M. Zhang, Y. Wang, J.F. Griffith, L. Qin, Journal of Orthopaedic Translation 2 (2014) 91–104.

1065 [74] S. Huang, L. Xu, Y. Sun, T. Wu, K. Wang, G. Li, Journal of Orthopaedic Translation 3 (2015)
1066   26–33.

1067 [75] Y.-Y. Jia, J.-Y. Zhou, Y. Chang, F. An, X.-W. Li, X.-Y. Xu, X.-L. Sun, C.-Y. Xiong, J.-L.
1068   Wang, Chin Med J (Engl) 131 (2018) 2089–2096.

1069 [76] V.D. Desai, H.C. Hsia, J.E. Schwarzbauer, PLOS ONE 9 (2014) e86865.

1070 [77] J. Hu, H. Liao, Z. Ma, H. Chen, Z. Huang, Y. Zhang, M. Yu, Y. Chen, J. Xu, Sci Rep 6 (2016).

1071 [78] R.A. Denu, S. Nemcek, D.D. Bloom, A.D. Goodrich, J. Kim, D.F. Mosher, P. Hematti, Acta
1072   Haematol 136 (2016) 85–97.

1073 [79] A.P. Croft, J. Campos, K. Jansen, J.D. Turner, J. Marshall, M. Attar, L. Savary, C. Wehmeyer,
1074   A.J. Naylor, S. Kemble, J. Begum, K. Dürholz, H. Perlman, F. Barone, H.M. McGettrick,
1075   D.T. Fearon, K. Wei, S. Raychaudhuri, I. Korsunsky, M.B. Brenner, M. Coles, S.N. Sansom,
1076   A. Filer, C.D. Buckley, Nature 570 (2019) 246–251.

1077

1078
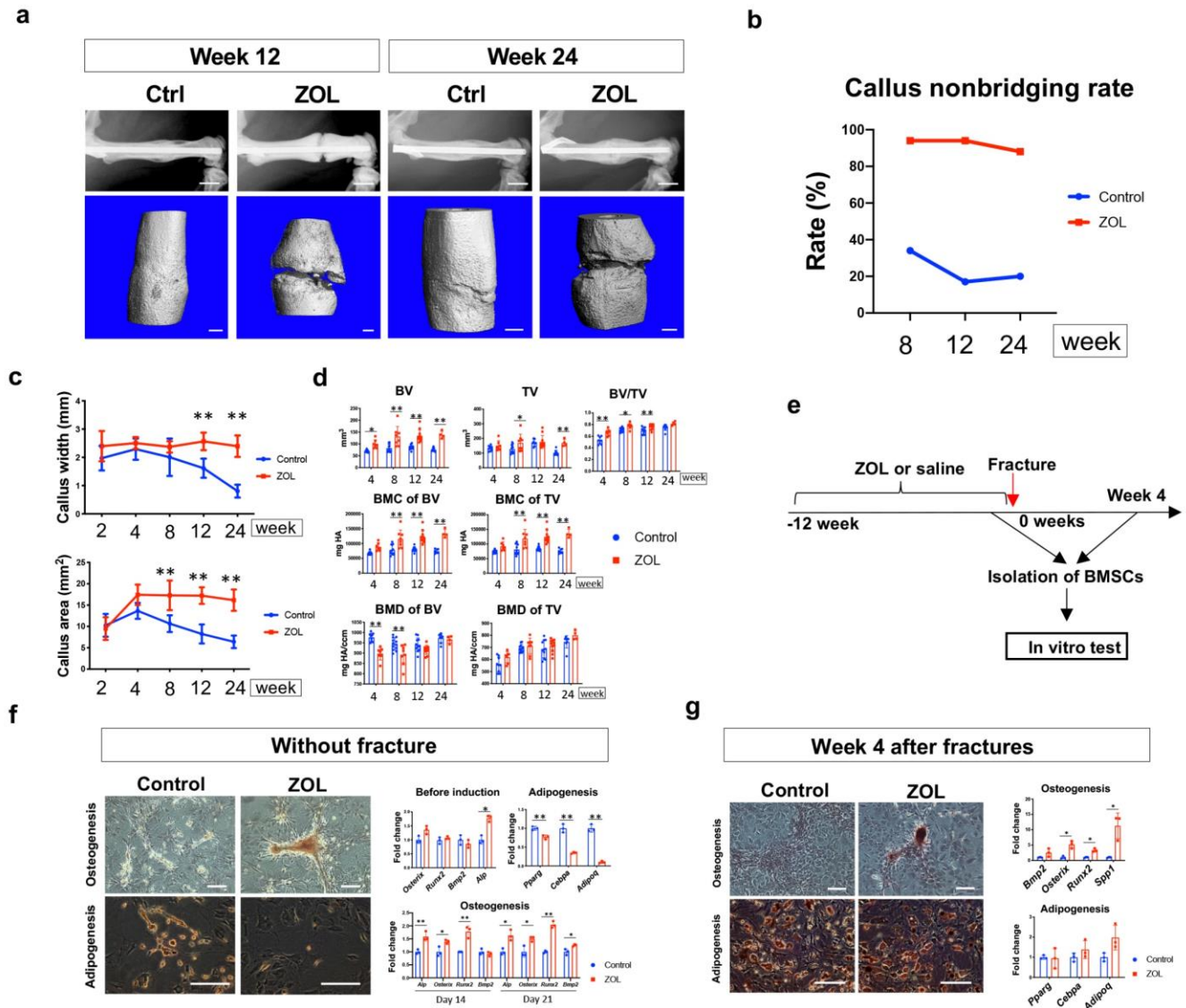
Fig. 1

Fig. 1. Impaired fracture healing in a rat model with long-term BPs treatment. a, Zoledronate

(ZOL) treatment induced non-bridging of fracture gap as shown by X-ray (upper panel, scale bar,

5 mm) and micro computed tomography (μCT, lower panel, scale bar, 1 mm). **b,** The non-healing

rate of ZOL-treated rats at week 12 and 24 was 94% and 88%, respectively (Table S1). **c,**

Radiograph-based analysis (n = 4) showed ZOL group presented with increased callus area and

callus width up to week 24 post-fracture. **d,** μCT-based quantification (n = 4-6) of the fracture gap.

1086 **e,** Schematic illustration of the isolation of bone marrow stem cells (BMSCs) before and after

1087 fractures for *in vitro* tests. **f and g,** Bone mesenchymal stem cells (BMSCs) harvested from intact

1088 and fractured femora of ZOL-pretreated rats exhibited increased osteogenic potential compared to

1089 the control group. Alizarin Red S staining and Oil Red S staining were used to stain calcium

1090 nodules and lipid droplets, respectively (scale bar, 200 μm). Gene expression level was assessed

1091 by RT-PCR (n = 3). Data were presented as mean ± SD. Two-way ANOVA with Sidak's *post hoc*

1092 test was used to analyze the data between each group at each time point except PCR results which

1093 were analyzed using Student's t test. * P < 0.05, ** P < 0.01.

1094

1095

1096

1097

1098

1099

1100

1101

1102

1103

1104

1105

1106
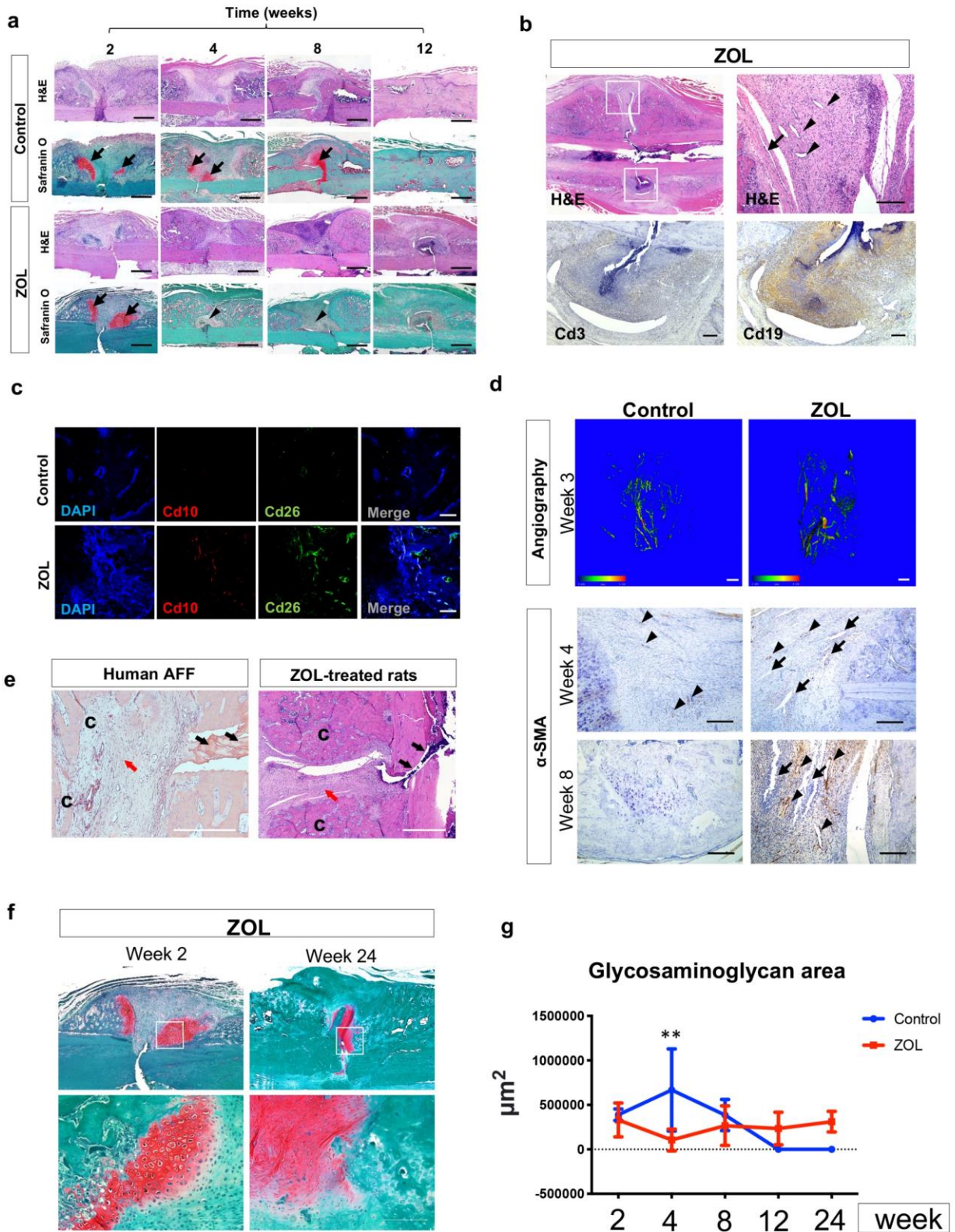
Fig. 2

Fig. 2. Aberrant fibrosis in non-bridged fracture gap of ZOL-treated rats. a, Hematoxylin and eosin stain (H&E) and safranin O staining of fractured bones showed the non-united fracture gap of ZOL-treated rats was characterized by fibrosis (arrowhead) and early disappearance of cartilaginous tissue (arrow). Scale bar, 400 μm. **b,** Prominent fibrous tissues (arrow) and vessel formations (arrowhead) in the non-bridged fracture gap of ZOL group at week 12 post-fracture (upper panel); Lymphocytes (Cd3 positive T cells and Cd19 positive B cells) indicative of chronic inflammation were found within the fracture gap (lower panel). Scale bar, 200 μm. **c,** Immunofluorescence staining showed increased retention of Cd26 and Cd10 positive fibroblasts in the fracture site of ZOL-pretreated rats (ZOL) group compared to the control group (Ctrl). Scale bar, 200 μm. **d,** Representative angiography (upper panel) showed disorientated vessels within the fracture gap of ZOL group at week 3 post-fracture. Scale bar, 1 mm; Immunohistochemistry staining (lower panel) revealed less functional arteries (α-SMA positive, arrowhead), while more abnormal vessel-like structures (arrow) in the ZOL group compared to the control group. Scale bar, 200 μm. **e,** c, external callus; red arrow, fibrous tissues; black arrow, amorphous acellular materials and cortical fragments. Scale bar, 1000 μm for human sample; 300 μm for rat sample. **f,** Safranin O staining. Lower panel pictures are the high-power images of the rectangle region of interests shown in the upper panel. Scale bar, 200 μm. Note the smooth transitional layers between the cartilaginous tissues and the surrounding fibrous tissues at 24 wpf. **g,** Calculation of the area of glycosaminoglycan-rich region. n = 3-6. Data were presented as the mean ± SD. Two-way ANOVA with Tukey's *post hoc* test was used to compared data between each group at week 2, 4, and 8. * $P < 0.05$, **: $P < 0.01$.
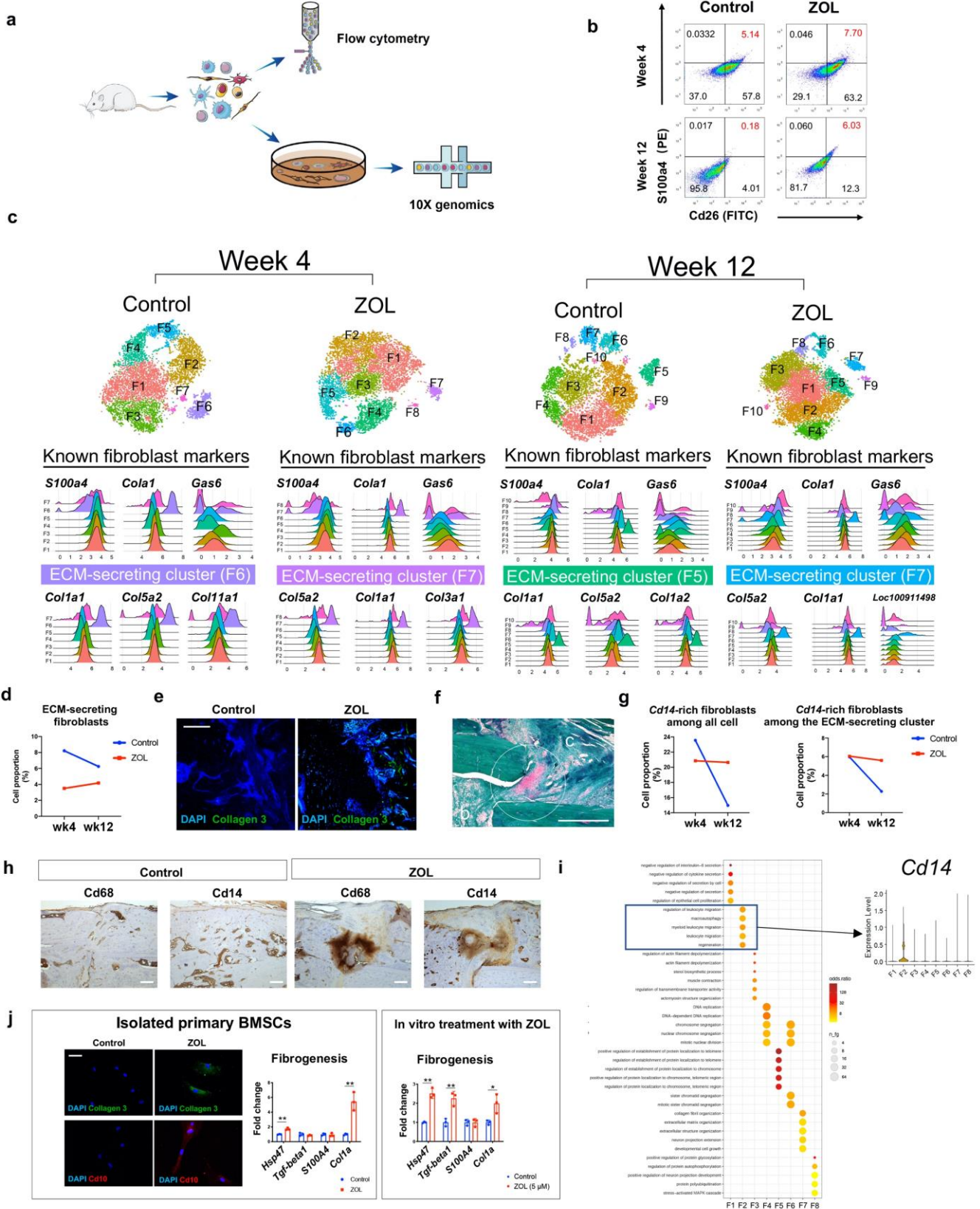
Fig. 3

1130

Fig. 3. ZOL prevented the clearance of extracellular matrix-secreting fibroblasts. a, Fracture

callus cells at week 4 and 12 post-fracture were digested for flow cytometry. In addition, isolated

cells were seeded on Petri dish and sent for scRNA-seq using 10x genomics in 24 hours after cell

attachment. **b,** Flow cytometry results of the proportion of S100a4/Cd26 double-positive

fibroblasts in the fracture callus at week 4 and 12 post-fracture. **c,** Upper panel: scRNA-seq

revealed heterogenous cell clusters on t-distributed stochastic neighbor embedding (t-SNE) plot

(upper panel). Middle panel: all the populations were fibroblasts based on expression of known

fibroblast markers (Fig. S5A). Lower panel: a unique cluster existed in across all groups, the gene

markers of which were associated with extracellular matrix (ECM) production. The top 3

expression markers for each group were plotted. For details refer to Fig. S3, S4. **d,** scRNA-seq

based calculation of the fraction of ECM-secreting fibroblasts cluster among the control and ZOL

group. Clear rate = (fraction of ECM-secreting fibroblasts at week 4 - fraction of ECM-secreting

fibroblasts at week 12) / fraction of ECM-secreting fibroblasts at week 4. **e,** Immunofluorescence

staining of collagen 3 in the non-bridged callus. Scale bar, 200 μm**. f,** Safranin O staining of

fracture site of ZOL group rats on 8 wpf. b, bone marrow cavity; c, the fibrosis tissues in the non-

bridged external callus; white circle, the glycosaminoglycan-rich fibrocartilages. Scale bar, 750

μm**. g,** scRNA-seq based calculation of the number of *Cd14*-positive fibroblasts among all cells

(left panel) or ECM-secreting fibroblasts (right panel). **h,** Immunohistochemical staining of Cd68

and Cd14 in the fracture gaps. Scale bar, 200 μm**. i,** Gene Ontology (GO) analysis of DEGs

between clusters showed that ZOL group contained a unique cluster (F2) at 4 wpf, which regulated

inflammation and was enriched for myeloid marker *Cd14* (Fig. S8). Significant level defined as P

< 0.05, one-sided Fisher's exact tests. **j,** Left panel: Fibrogenesis of BMSCs harvested form ZOL-

pretreated rats at 4 wpf. Immunofluorescent staining (left, scale bar, 50 µm) was used to detect expression of collagen 3 and Cd10 on day 10 of fibrogenesis and quantitative RT-PCR was used to assess fibrogenic gene expression (right) at the same time point. Right panel: *in vitro* treatment with ZOL-conditioned fibrogenic medium (ZOL concentration, 5 µM) of rat BMSCs isolated from the control group rats at 4 wpf. Gene expression was measured by quantitative PCR on day 10 of induction. Data were presented as the mean ± SD. Student's t test. n = 3. * $P < 0.05$, ** $P < 0.01$.
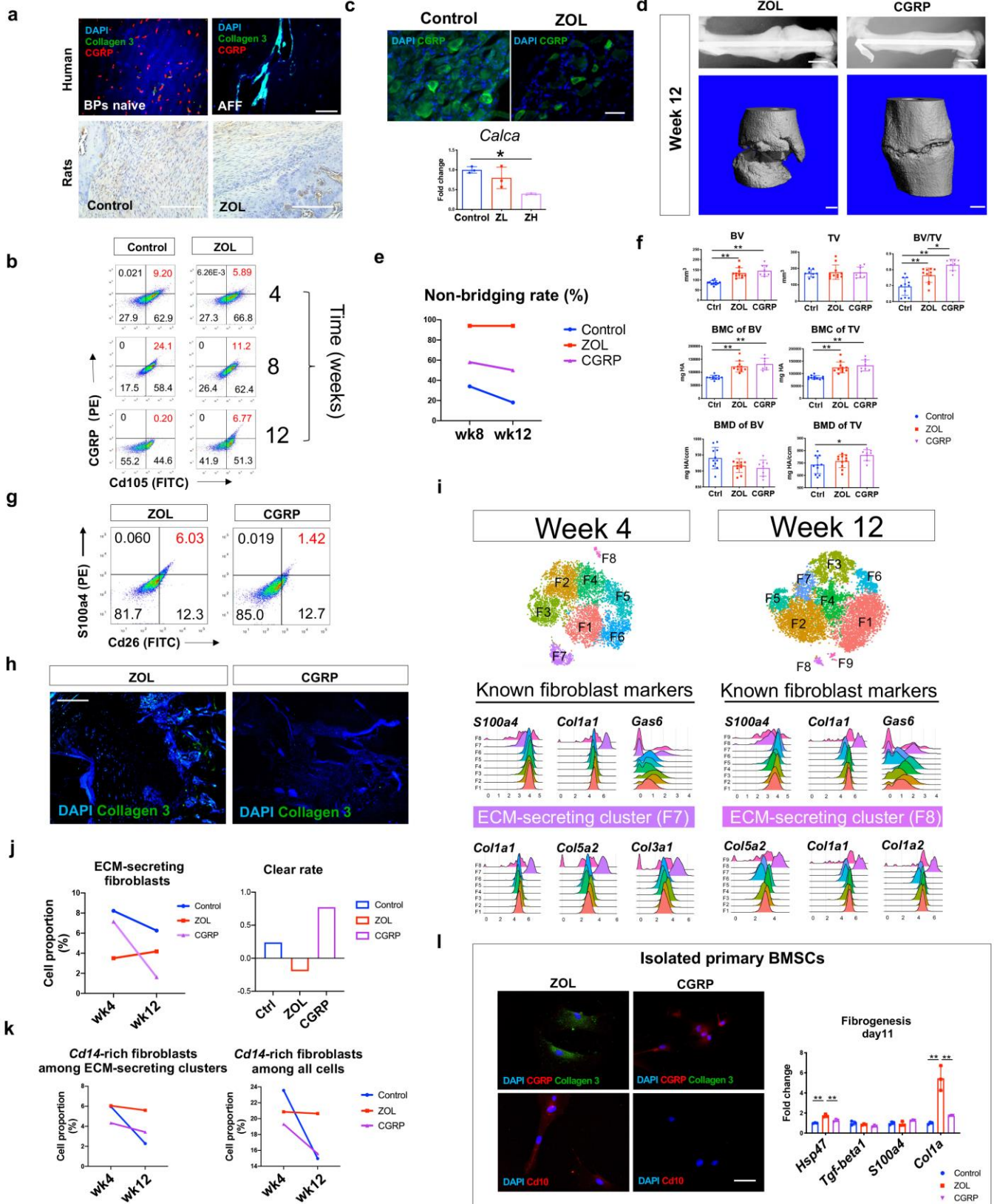
Fig. 4

1176

Fig. 4. Restoration of CGRP promoted fracture healing. a, Upper panel: Immunofluorescent staining of CGRP and collagen 3 on human AFF specimen. Lower panel: Immunohistochemical staining of CGRP on rat samples with long-term BPs treatment at 4 wpf. Scale bar, 200 μm. **b,** Flow cytometry for CGRP/Cd105 double-positive cells in the fracture callus in the control and ZOL group at 4 and 8 wpf. **c,** Upper panel: Immunofluorescent images of CGRP expression in DRG at 4 wpf. Scale bar, 50 μm. Lower panel: RT-PCR results for CGRP expression in primary DRGs *in vitro* treated with either low (500 nM, ZL) or high concentration (5 μM, ZH) of ZOL for 2 days. n = 3. **d,** X-rays (upper panel, scale bar, 5 mm) and 3D reconstruction of CT data (lower panel, scale bar, 1 mm). **e,** Radiograph-based calculation of non-bridging rate (Table S3). **f,** Quantitative CT data of the fractured bone, n = 4-6. **g,** Flow cytometry for S100a4/Cd26 double-positive cells in the fracture callus of the control and CGRP group rats. **h,** Immunofluorescent staining of collagen 3 in CGRP-treated rats at 12 wpf. Scale bar, 200 μm. **i,** scRNA-seq of fracture callus cells from CGRP group revealed the presence of the ECM-secreting fibroblast cluster at 4 (F7) and 12 (F8) wpf, respectively (lower panel). All clusters were identified as fibroblasts (middle panel; Fig. S12, S13a) and visualized on t-SNE (upper panel). **j,** The fraction (left) and clearance rate (right) of ECM-secreting fibroblasts based on scRNA-seq. Clear rate = (fraction of ECM-secreting fibroblasts at week 4 - fraction of ECM-secreting fibroblasts at 12 wpf) / fraction of ECM-secreting fibroblasts at 4 wpf. **k,** The fraction of *Cd14*-positive fibroblasts among the ECM-secreting fibroblasts (left panel) and all fibroblasts (right panel) during fracture healing based on scRNA-seq. **l,** Left: immunofluorescent staining of CGRP, collagen 3, and Cd10 in BMSCs isolated from CGRP group that underwent fibrogenic induction for 10 days *in vitro*. Right: RT-PCR results of fibroblast-related gene expression at the same time point. Scale bar, 50 μm. Data

1199   were presented as mean ± SD. Statistical analysis was performed using one-way ANOVA with

1200   Tukey's *post hoc* test. * P < 0.05, ** P < 0.01.

1201

1202

1203

1204

1205

1206

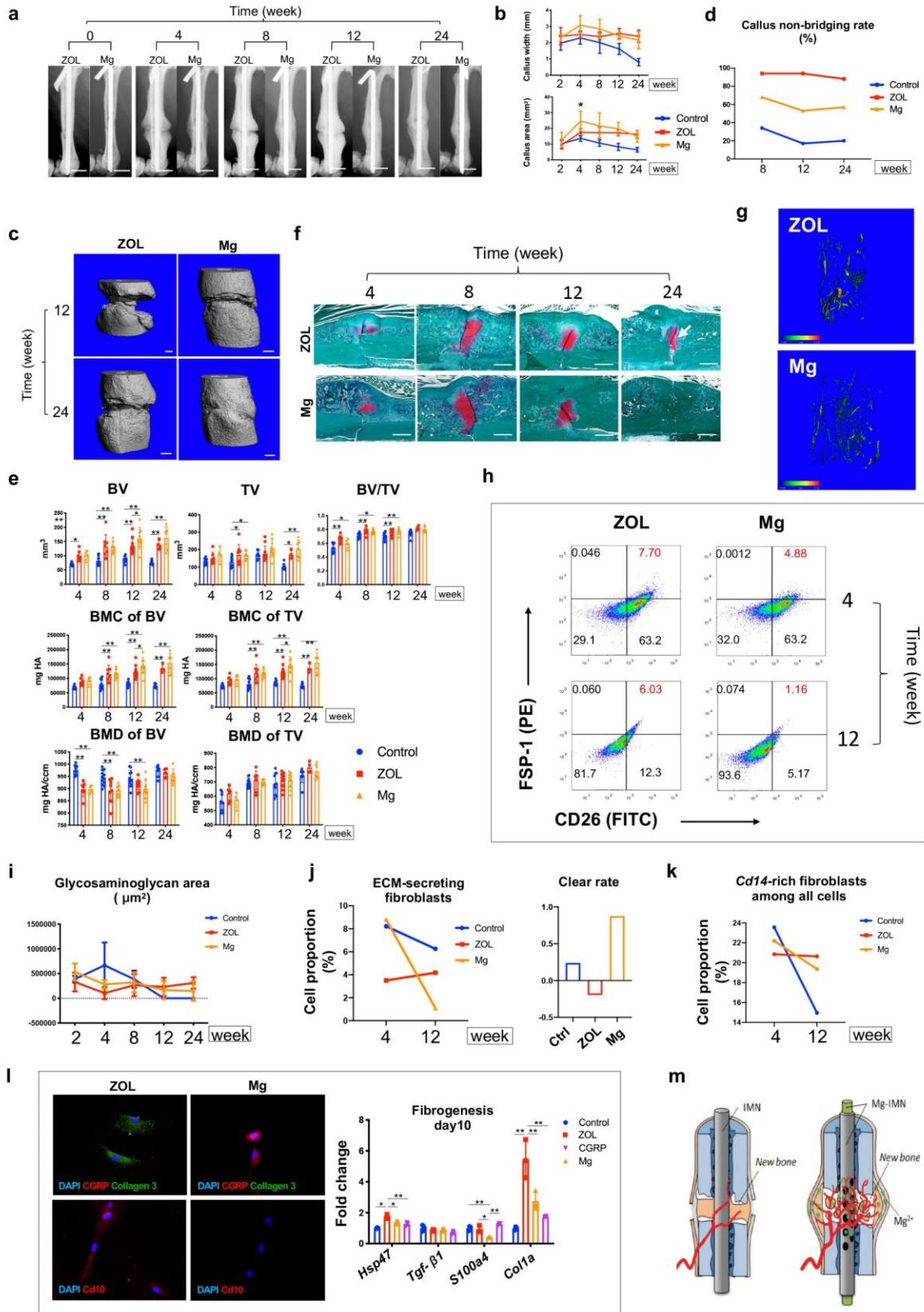1207

1208

1209

1210

1211

1212

1213

1214

1215

1216

1217

1218

1219

1220

1222

Fig. 5. Enhanced fracture healing by Mg-IMN. a, Representative X-rays of ZOL-pretreated rats fixed with Mg-IMN (Mg group). Scale bar, 5 mm. **b,** X-ray-based calculation of callus area and callus width, n = 4-6. **c,** Representative μCT reconstruction of Mg group rats. Scale bar, 1 mm. **d,** Radiograph-based calculation of callus non-bridging rate. **e,** Quantitation of μCT data of Mg group rats, n = 4-12. **f,** Safranin O staining of Mg group rats. White arrow: the retained cartilages. Scale bar, 400 μm**. g,** CT-based angiograph of Mg-treated rats. Scale bar, 1 mm. **h,** Flow cytometry for S100a4/Cd26 double-positive fibroblasts (red circles) in rats fixed with Mg-IMN reduced the proportion of S100a4/Cd26 double-positive fibroblasts in the fracture callus. **i,** Quantitative analysis of safranin O-stained area, n = 3-5. **j,** The fraction and clearance rate of ECM-secreting fibroblasts based on scRNA-seq analysis. **k,** The fraction of fibroblasts enriched for *Cd14* among the fracture calluses. **l,** Fibrogenic induction of BMSCs isolated from Mg group rats at 4 wpf. Left panel: Immunofluorescent staining of collagen 3, Cd10, and CGRP on day 10 of fibrogenic induction. Scale bar, 50 μm. Right panel: RT-PCR results of fibrogenic gene expression on day 10 of induction. n = 3. Data were presented as mean ± SD. **m,** Schematic diagram of the Mg-IMN. The pure Mg pin inside the stainless-steel IMN (SS-IMN) gradually released Mg ions through the vents into surrounding bone tissues to stimulate the release of CGRP, which in turn promoted bone formation and angiogenesis while prevented fibrosis. Statistical analysis, **b, e, i,** two-way ANOVA with Sidak's *post hoc* test to compared between each group at each time point; **l,** One-way ANOVA with Tukey's *post hoc* test. * P < 0.05, ** P < 0.01.

1242

1243   **Fig. 6**
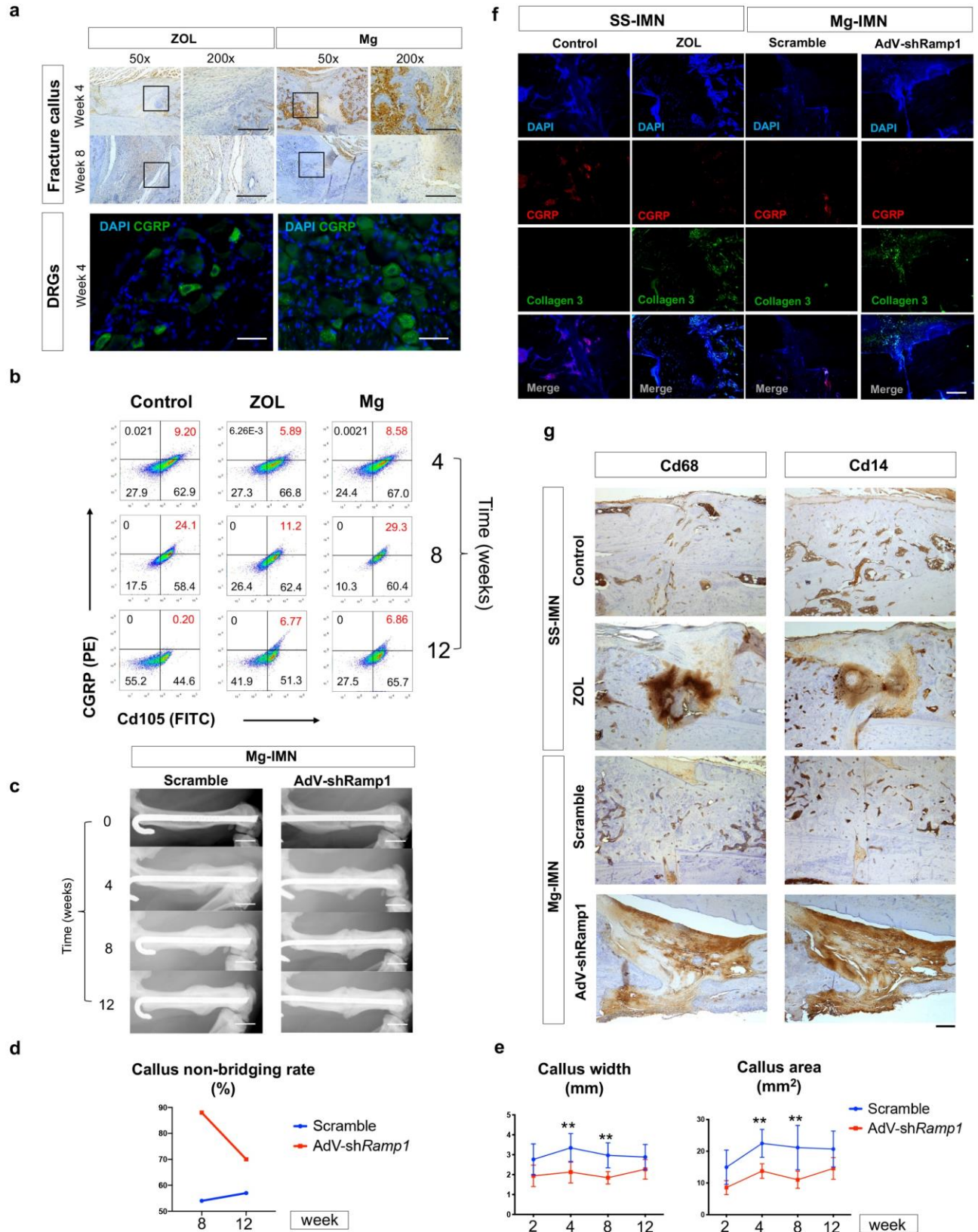
Fig. 6. The role of CGRP in the Mg-facilitated healing. a, Upper panel: immunohistochemical staining (upper panel) of CGRP in fracture callus of rats fixed with Mg-IMN (Mg group). Scale bar, 200 μm. Lower panel: immunofluorescent staining of CGRP in DRGs from Mg group. Scale bar, 50 μm. **b,** Flow cytometry for CGRP/Cd105 double-positive cells in the fracture callus. **c,** Radiograph showed that *Ramp1* shRNA-adenovirus treated rats (AdV-shRamp1) displayed non-bridged fracture gaps at 12 wpf, opposing to scramble group where callus bridged smoothly. Scale bar, 5 mm. **d,** Radiograph-based calculation of callus non-bridging rate. **e,** Quantitative analysis of callus area and callus width based on X-ray images, n = 6. **f,** Immunofluorescent staining of collagen 3 in the fracture gap of AdV-shRamp1 and scramble group. Scale bar, 200 μm. **g,** Immunohistochemical staining of myeloid markers Cd14 and Cd68 in the fibrotic fracture gap of AdV-shRamp1 group at 12 wpf. Scale bar, 200 μm. Data were presented as mean ± SD. Statistical analysis were performed using two-way ANOVA with Sidak's *post hoc* test to compare between each group at each time point. * $P < 0.05$, ** $P < 0.01$.

Fig.7
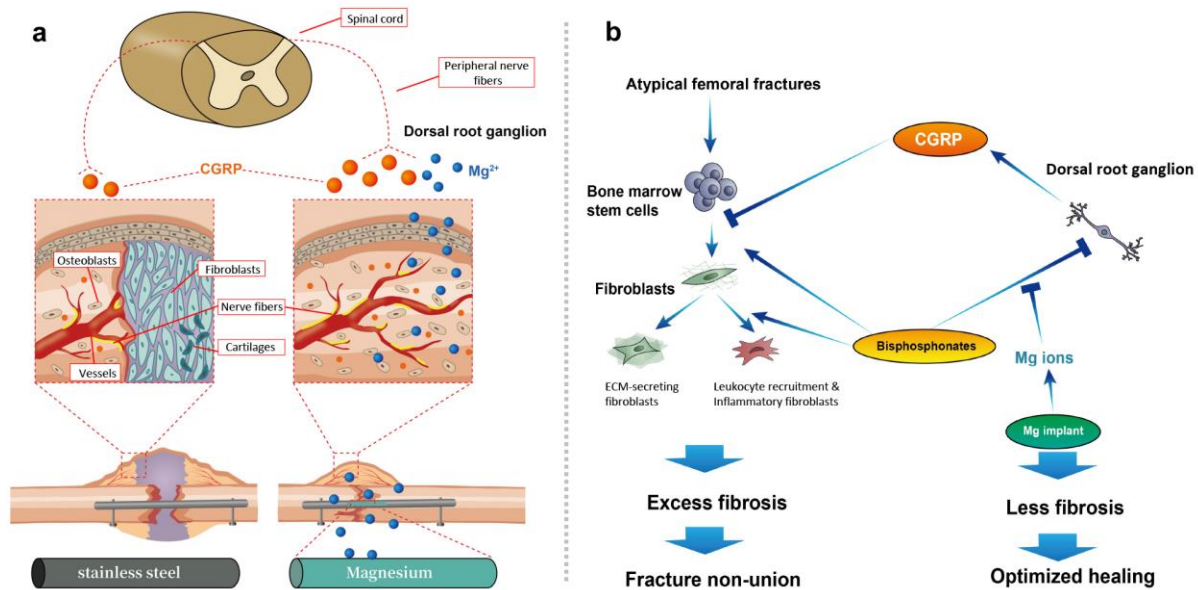
Figure 7. Schematic illustration showing the beneficial effect of Mg-IMN in treating BPs-associated AFFs. a, Mg ions released from the magnesium containing intramedullary nail (Mg-IMN) stimulates CGRP release from the dorsal root ganglion into the fracture site, resulting in optimized neovascularization, lesser fibrosis, and bridging of the fracture callus. **b,** At cellular level, long-term BPs treatment diverts bone marrow stem cells (BMSCs) into a fibroblastic cell fate by a direct effect of BPs as well as BPs-induced reduction in CGRP release from the dorsal root ganglion. This leads to an increase in number of pathogenic fibroblasts that actively secret extracellular matrix and/or mediate inflammation, contributing to excess fibrosis and non-union of AFFs. Mg-IMN, in contrast, promotes AFF healing by stimulating CGRP release.

CRediT author statement of

Magnesium Facilitates the Healing of Atypical Femoral Fractures: A Single-cell Transcriptomic Study

(Ref. MATTOD-D-21-00954)

Nianye Zheng: Conceptualization, Methodology, Software, Validation, Formal analysis, Investigation, Data Curation, Writing - Original Draft, Writing - Review & Editing, Visualization. **Jiankun Xu**: Conceptualization, Methodology, Validation, Formal analysis, Investigation, Writing - Original Draft, Writing - Review & Editing, Visualization, Supervision, Funding acquisition. **Ye Chun Ruan**: Conceptualization, Methodology, Visualization. **Liang Chang**: Investigation. **Xinluan Wang**: Methodology, Validation**. Hao Yao**: Validation, Investigation. **Jiali Wang**: Investigation. **Ri Zhang**: Investigation. **Qingyun Xue**: Conceptualization. **Ning Tang**: Resources. **Tim-yun Ong**: Resources. **Jörg Schilcher**: Resources, Writing - Original Draft. **Regis J. O'Keefe**: Conceptualization, Methodology, Writing - Original Draft, Supervision, Project administration. **Ling Qin**: Conceptualization, Methodology, Writing - Original Draft, Writing - Review & Editing, Supervision, Project administration, Funding acquisition.

Click here to access/download
Supplementary Material
Supplementary information_rv_1.docx

Declaration of interests

☒ The authors declare that they have no known competing financial interests or personal relationships that could have appeared to influence the work reported in this paper.

☒The authors declare the following financial interests/personal relationships which may be considered as potential competing interests:

Nianye Zheng, Jiankun Xu, Yechun Ruan, Liang Chang, Xinluan Wang, Hao Yao, Jiali Wang, Ri

Zhang, Qingyun Xue, Ning Tang, Tim-yun Ong, Jörg Schilcher, Regis J. O'Keefe, Ling Qin